ABSTRACT

Title of dissertation:	X-RAY ASTROPHYSICS: CONSTRAINING THERMAL CONDUCTIVITY IN INTRACLUSTER GAS IN CLUSTERS OF GALAXIES AND PLACING LIMITS ON PROGENITOR SYSTEMS OF TYPE IA SUPERNOVAE
	Brock Richard Russell, Doctor of Philosophy, 2014
Dissertation directed by:	Professor Gregory Sullivan Department of Physics

X-ray astrophysics provides a great many opportunities to study astronomical structures with large energies or high temperatures. This dissertation will describe two such applications: the use of Swift X-ray Telescope (XRT) data to analyze the interaction between a supernova shock and the circumstellar medium, and the use of a straightforward computer simulation to model the dynamics of intracluster gas in clusters of galaxies and constrain the thermal conduction coefficient.

Stars emit stellar wind at varying rates throughout their lifetimes. This wind populates the circumstellar medium (CSM) with gas. When the supernova explodes, the shock wave propogates outward through this CSM and heats it to X-ray emitting temperatures. By analyzing X-ray observations of the immediate post-supernova environment, we are able to determine whether any significant CSM is present. By stacking a large number of Swift observations of SNe Ia, we increase the sensitivity. We find no X-rays, with an upper limit of 1.7×10^{38} erg s^{-1} and a 3σ upper limit

on the mass loss rate of progenitor systems 1.1×10^{-6} M$_\odot$ yr^{-1} $\times$ $(v_{\rm w})/(10$ km s$^{-1})$. This low upper limit precludes a massive progenitor as the binary companion in the supernova progenitor system, unless that star is in Roche lobe overflow.

The hot Intracluster Medium (ICM) is composed of tenuous gas which is gravitationally-bound to the cluster of galaxies. This gas is not initially of uniform temperature, and experiences thermal conduction while maintaining hydrostatic equilibrium. However, magnetic field lines present in the ionized gas inhibit the full thermal conduction. In this dissertation, we present the results of a new one-dimensional simulation that models this conduction (and includes cooling while maintaining hydrostatic equilibrium). By comparing the results of this model with the observed gas temperature profiles and recent accurate constraints on the scatter of the gas fraction, we are able to constrain the thermal conductivity. Our results suggest that conduction factors are not higher than 10% of full Spitzer conduction for hot, relaxed clusters.

X-RAY ASTROPHYSICS: CONSTRAINING THERMAL CONDUCTIVITY IN INTRACLUSTER GAS IN CLUSTERS OF GALAXIES AND PLACING LIMITS ON PROGENITOR SYSTEMS OF TYPE IA SUPERNOVAE

by

Brock Richard Russell

Dissertation submitted to the Faculty of the Graduate School of the
University of Maryland, College Park in partial fulfillment
of the requirements for the degree of
Doctor of Philosophy
2014

Advisory Committee:
Professor Gregory Sullivan, Chair/Advisor
Dr. Maxim Markevitch, Co-Advisor
Professor William Dorland
Professor Douglas Hamilton
Professor Chris Reynolds

Table of Contents

List of Figures

Chapter 1: Introduction

1.1 Introduction

The field of X-ray astrophysics is relatively young, and as such there is a lot of opportunity for scientific progress. Astrophysical X-rays do not penetrate the atmosphere of the Earth, so some means of moving the detector above a significant part of the atmosphere is necessary in order to make X-ray astrophysics even possible. The first detection of X-rays from space was in a sounding rocket test flight in 1949, in which solar X-rays were detected, followed by other rocket flights. These had several limitations, however, as they were only aloft for short periods of time. In 1962, the first extra-solar X-ray detection was made. Balloons were also used for X-ray detection, since they are able to float above a large portion of the atmosphere. These were employed from the 1960s. There was even the use of rockoons, which are rockets that are lifted to high altitudes by balloons then ignited to rise to even higher levels. [Arnaud, et al.(2011)]

X-ray astronomy really took off with the launch of astronomical satellites. The first X-ray satellite telescope was Uhuru, launched in 1970. Uhuru was followed by a series of X-ray satellites, including the Einstein Observatory, Exosat, and Rosat. Currently operating X-ray satellites include Swift, Chandra, XMM-Newton, and

Suzaku. [Arnaud, et al.(2011)]

Early X-ray detectors relied on proportional counters. These devices use a contained gas surrounding an anode kept at a positive voltage. When an X-ray photon enters the gas, it creates a number of electron-ion pairs proportional to the energy of the incident radiation. These electrons are attracted to the anode, and the number of electrons collected by the anode is proportional to the energy of the incoming X-ray (hence the name). Some positioning techniques can be employed to allow some imaging with proportional counters. [SC(2008)]

Today, X-ray telescopes use CCDs, in which an incoming X-ray photon ionizes the detector materials and the charge is read directly. A new type of detector, the quantum calorimeter, was planned for the Suzaku mission. This detector measured the increase in temperature of a crystal caused by the absorption of an X-ray photon. It requires that the crystal be maintained a very low temperatures (< 0.1 K), though, and due to problems with the refrigerator on Suzaku, this detector was not able to be used for astronomy. [SC(2008)]

To determine the direction of the incoming photons, in order to form images of the sky, early X-ray detectors limited their field of view via slat collimators, and simply scanned over the sky with a small field of view to form images. Another method is the coded mask, in which a sheet of material that is opaque to X-rays is placed in front of the detector element. This creates a shadow on the image which matches a particular point on the mask, and the position can be determined from this. This method is employed by the Swift Burst Alert Telescope (BAT), which can observe a large portion of the sky at once to look for gamma-ray bursts.

X-ray satellites rely on special optics because of the physics of the X-ray photons themselves. Since X-rays are particularly energetic, they would pass through most usual lens materials. Instead, total external reflection is employed, where the critical angle is determined via Snells Law and can be written as [Schwartz(2011)]:

$$\theta_c \propto \sqrt{Z}/E \qquad (1.1)$$

where Z is the atomic number of the reflecting material and E is the energy of the X-ray photon. Because high Z leads to larger critical angle, gold, platinum, and iridium are often used, and nickel and polished quartz have also been used. [[SC(2008)], [Schwartz(2011)]] The mirrors are arranged so that incoming X-ray photons first reflect off a parabolic mirror section, then off a hyperbolic mirror segment. Several of these pairs of mirror segments are nested to increase the effective area of the detector [SC(2008)]

These mirrors have small imperfections, partly due to the fabrication process and partly due to the accumulation of dust in orbit. These imperfections lead to scattering of the photons, and cause the image of a point source on the detector to appear as a bright point surrounded by a halo. The point spread function (PSF) is used to define this spreading of the brightness. [SC(2008)]

Proportional Counters and CCDs can be used to obtain spectra. However, the use of diffraction gratings allows for much greater energy resolution. The materials in the grating must be of sufficiently dense matter so that they are not transparent to the X-rays. Gold is used in the Chandra transmission gratings, of which there

are three sets that can be placed in the beam when required. XMM-Newton uses reflection gratings in two of the three detectors. These gratings are not able to be removed from the beam. [SC(2008)]

In X-ray astrophysics, in particular in supernova astrophysics using X-rays, the photon detection rate can be very low. Detection rates of as low as 10^{-4} counts per second are not uncommon, after correcting for background. However, this detection is sufficiently above background levels and does allow some statistical analysis. This will be discussed in the appropriate chapter.

A large range of astrophysical topics benefit from X-ray astrophysics, including Active Galactic Nuclei, supernova remnants, black holes, etc. In this dissertation, I will describe two research projects involving X-ray astrophysics. In the first section, I will describe the use of X-rays to probe the circumstellar medium surrounding stars just after they explode as supernovae. This analysis provides useful information about massive stars that explode as core-collapse supernovae, but also we can learn interesting information about Type Ia supernovae as well. This is important given the role of Type Ia supernovae as standard candles. The second major project that I will discuss involves a computational study of the dynamics in the hot intracluster gas in clusters of galaxies. These gasses have very high temperatures and X-ray observations are used to determine the thermal profile and density distribution of this gas. The computational study focuses on the temporal evolution of this gas, and the results of the study are used to constrain certain parameters of the thermal conduction in the gas.

There are several mechanisms by which X-rays can be produced in astrophys-

ical settings. The one I will be focusing on in this work is thermal bremsstrahlung radiation. In this case, hot gas in thermal equilibrium at a high temperature ($> 10^6$ K) consists of electrons and ions. When an electron passes near an ion, it experiences an acceleration that changes its direction. These accelerations cause the electrons to emit photons of varying energies, which at these high temperatures are significantly in X-ray energies. Some electrons can also collide with and transfer energy to ions, causing the electronic structure within the ions to move to higher energy levels. When these ions decay back down to a lower state, a photon is emitted, resulting in line emission. This can occur at temperatures below approximately 5×10^7 K, since above these temperatures the gas is almost completely ionized. [SC(2008)]

Synchrotron radiation can occur when relativistic electrons are present in a region with magnetic fields. As the electrons experience the magnetic force and are therefore accelerated, they emit photons with energy determined by the speed of the electrons and the strength of the magnetic field. Blackbody radiation is emitted by starlike objects at a temperature T, and when the temperature is high enough, a significant number of X-rays can be emitted. Various other objects, such as planets, moons, and asteroids, can also emit X-rays after being impacted by energetic particles. An additional source of astrophysical X-rays is inverse Compton scattering of photons. When a lower energy photon collides with an energetic electron, the photon can be Compton scattered to X-ray energies. [SC(2008)]

In Chapter 2, I will describe the physics of supernovae, including a brief overview of stellar evolution before the supernova, with emphasis on the relevant pieces. Chapter 3 will describe the analysis methods applied to X-ray observations

of Type Ia Supernovae, as well as the results obtained from this analysis. Chapter 4 begins the section of clusters of galaxies, and includes background on the physics present in these large gravitationally-bound systems. Chapter 5 describes the numerical methods used to model the behavior of the hot intracluster gas, and Chapter 6 presents the results of these simulations. Also in Chapter 6, I will compare these results to observations of current clusters of galaxies to constrain the thermal conduction suppression factor present in the intracluster medium (ICM).

Chapter 2:   Supernovae – Introduction

A supernova (SN, plural SNe) is the final stage of stellar evolution for certain stellar types. It is a very powerful explosion. There are two primary types of supernovae, which for historical reasons are known as Type Ia and Type II. There are also Type Ib/c, which are similar in many ways to Type II. In general, X-ray observations of supernovae are possible because stars emit stellar wind over their lifetimes. This populates the so-called circumstellar medium (CSM) with gas at a density that depends on the stars mass-loss rate and the speed of the stellar wind. When a SN occurs, its shockwave plows into this CSM and heats it to very high temperatures. These temperatures are often high enough that the matter emits X-rays, which we then detect via various instruments. The information from these observations can be combined with reasonable assumptions about the nature of the wind itself to reach conclusions about the historic mass-loss rates of the SN progenitor system.

Type II supernovae occur in the late stages of massive stars. The intense pressure and temperature begin to fuse heavier elements together to create certain elements necessary for our life. However, when this fusion process begins to shut down, there is less pressure holding the star up. It collapses in on itself until enough

energy is built up to explode outward.

SNe Ia are generally considered to be thermonuclear explosions of white dwarfs (WDs) (e. g. [Hillebrandt & Niemeyer(2000)]). Such explosions can occur if the WD reaches or exceeds the Chandrasekhar mass limit, although some models suggest that the explosion can occur below the Chandrasekhar limit ([van Kerkwijk et al.(2010)], for example). There are currently two main classes of models for possible progenitor systems for SNe Ia [Hillebrandt & Niemeyer(2000)]: 1.) one white dwarf accretes mass from a binary companion until it exceeds the Chandresekhar limit ([Whelen & Iben(1973), Iben & Tutukov(1984), Nomoto(1982)]; single-degenerate, SD model) and 2.) two white dwarfs merge ([Webbink(1984), Iben & Tutukov(1984)]; double-degenerate, DD model). In the SD model, the companion star emits a stellar wind that populates the circumstellar region with matter, or the star fills the Roche lobe [Branch(1998)]. The SN shock would run into this circumstellar matter and heat it to high enough temperatures ($\sim 10^6 - 10^9$ K) so that it produces thermal X-rays, depending on the fraction accumulated by the white dwarf [Chevalier(1990)]. For the DD model both stars in the binary system have long ago ceased producing significant wind, and therefore the circumstellar region will be devoid of matter [Branch(1998)]. Hence, no thermal X-ray emission is expected from shock interaction.

Various observations and studies have been made in an attempt to determine which of these models is correct. In the SD model, there are several methods of mass transfer. One is the so-called "symbiotic" binary system, where a fraction of the wind from a binary companion is accreted by the WD until it reaches the Chandrasekhar limit [Panagia et al.(2006)]. [Panagia et al.(2006)] have put constraints

on this possibility by analyzing radio observations of a sizable sample of SNe Ia. See below for more discussion of their results. Another possible method of accretion is that of a massive binary in Roche lobe overflow with material again being accreted onto the WD [Panagia et al.(2006)]. [Panagia et al.(2006)] placed a limit on this, stating that such a method would be required to be $60 - 70$ % efficient to avoid detectable circumstellar matter (CSM). These limits rely on the conclusions of [Nomoto(1984)] regarding the conditions of accretion to allow a WD to become a SN Ia.

A VLA observation of SN 1986G looking for early radio emission resulting from the interaction of the SN shock with the wind from a red giant companion detected no such emission at 2 cm and 6 cm. The 3σ upper limits of 0.7 and 1.0 mJy, respectively, are in conflict with those expected from the symbiotic case [Eck et al.(1995)], although they point out that this was a "peculiar" SN Ia. [Panagia et al.(2006)] conducted a radio survey of 27 SNe Ia and detected no radio emission (with a highest radio luminosity upper limit of 4.2×10^{26} erg s^{-1}), therefore concluding that these systems have low CSM densities. They explicitly argue against the SD model for a massive companion, but state that their results do allow for a relatively low mass companion. They also provide 2σ upper limits for the mass loss rate for the system as 3×10^{-8} M$_\odot$ yr^{-1}, the lowest upper limits published to date (note that these limits are much higher than the mass-loss rate of the Sun by several orders of magnitude).

[Schlegel & Petre(1993)] have observed SN 1992A using ROSAT searching for X-rays. They establish an X-ray luminosity upper limit of $3 - 5 \times 10^{38}$ erg s^{-1} and a

mass loss rate upper limit of a few $\times 10^{-6}$ M$_\odot$ yr^{-1} [Schlegel & Petre(1993)]. [Hughes et al.(2007)] used the Chandra X-ray telescope to observe four SNe Ia. For two of the SNe Ia they observed (SN 2002bo and SN 2005ke), they detected no X-rays and obtained an upper limit of 2×10^{-5} M$_\odot$ yr^{-1} for 2002bo. For the other two (SN 2002ic and SN 2005gj), they find upper limits about 4 times lower than would be expected for circumstellar interaction, and propose a mixing scenario to increase X-ray absorption.

[Immler et al.(2006)] have determined relatively low upper limits on X-ray emission from SNe Ia using the *Swift* X-ray Telescope (XRT). They examined SN 2005ke, but found inconclusive evidence for X-ray emission. They determine upper limits of luminosity of $(2 \pm 1) \times 10^{38}$ erg s^{-1} and mass loss rate of 3×10^{-6} M$_\odot$ yr^{-1} $(v_w/(10 \text{ km s}^{-1}))$, the lowest upper limits published to date from X-ray observations.

[Hancock et al.(2011)] have stacked VLA radio data from 46 observations of nearby SNe Ia to create a deep image, and obtain a radio luminosity upper limit of 1.2×10^{25} erg s^{-1} Hz^{-1} at 5 GHz, and a mass-loss rate upper limit for the progenitor system of 1.3×10^{-7} M$_\odot$ yr^{-1}.

Our goal in Chapter 3 is to add to and expand on the previous X-ray studies. Of all past and present X-ray observatories, the *Swift* X-Ray Telescope has observed the largest sample of SNe in X-rays, with unprecedented early observations starting just days after outburst. We use data from XRT to determine an upper limit on X-ray luminosity from more than 50 SNe Ia, adding to the growing consensus regarding the progenitor systems of these events.

Chapter 3:   Type Ia Supernovae Methods and Results

3.1   Data

The X-Ray Telescope (XRT; [Burrows(2005)]) onboard the *Swift* telescope [Gehrels et al.(2004)] has observed more than 170 SNe to date. Of these, 55 are SNe Ia (at the time of this writing). In order to further narrow this sample to SNe most likely to produce detectable X-rays, we applied the following conditions for selection:

- Young: observations begin within 100 days of SN discovery;
- Nearby: distance to SN within 130 Mpc (using previously determined distances from NED (NASA/IPAC Extragalactic Database) and references therein);
- No contamination by nearby X-ray source: separation of SN position from nearby X-ray source $> 24''$ (corresponding to the XRT 90% encircled energy width).

These conditions lead to the selection of 53 of the SNe Ia that have been observed by the XRT in our calculations. They are listed in Table 1, along with their individual luminosity upper limits. Some of these are relatively high due to contamination from the galactic nucleus. All X-ray data used are in the 0.2-10 keV energy band, chosen due to parameters of the detector.

Table 1: Type Ia Supernova Properties

Supernova	Weighted Average Date [days after discovery]	Date Range [days after discovery]	Distance [Mpc]	Exposure Time [ks]	Luminosity (0.2-10 keV) 3σ upper limit $[10^{38}$ erg s$^{-1}]$	Mass Loss Rate 3σ upper limit $[\frac{10^{-6}M_\odot \mathrm{yr}^{-1}}{10\mathrm{km s}^{-1}}]$
2005am	55.9	$11.0 - 84$	30	71.7	20.2	9.0
2005bc	2.7	$2.7 - 2.7$	52	0.7	2184.2	20.7
2005cf	53.7	$7.0 - 462.4$	29	66.4	14.5	7.5
2005df	233.5	$6.1 - 860.5$	16	50.7	4.4	8.5
2005gj	831.7	$59.1 - 1257.1$	50	14.7	94.7	75.0
2005hk	187.0	$4.8 - 935.1$	56	57.7	39.3	22.9
2005ke	50.8	$1.7 - 1228.8$	19	288.3	2.7	3.2
2006dd	131.0	$1.8 - 120.2$	23	100.8	199.9	43.2
2006dm	142.2	$2.6 - 728.6$	87	80	145.7	38.4
2006E	126.3	$1.8 - 351.0$	11	31.8	4.4	6.3
2006ej	91.6	$1.8 - 490.7$	78	48.3	147.5	31.0
2006mr	54.2	$2.6 - 172.0$	23	56.6	238.3	30.3
2006X	26.1	$4.3 - 668.6$	17	58.9	5.4	3.2
2007af	68.1	$1.8 - 288.0$	25	125.6	10.3	7.1
2007ax	96.3	$8.8 - 576.0$	31	65.1	67.2	21.5
2007bm	214.9	$6.7 - 578.0$	26.3	28.4	38.5	24.3
2007co	115.9	$5.8 - 386.3$	99	54.8	276.7	47.8
2007cq	104.1	$4.7 - 390.4$	50	53.3	53.3	19.9

Table 1 (continued): Type Ia Supernova Properties

Supernova	Weighted Average Date [days after discovery]	Date Range [days after discovery]	Distance [Mpc]	Exposure Time [ks]	Luminosity (0.2-10 keV) 3σ upper limit $[10^{38}$ erg s$^{-1}]$	Mass Loss Rate 3σ upper limit $[\frac{10^{-6}M_\odot yr^{-1}}{10kms^{-1}}]$
2007cv	111.4	$1.8 - 404.0$	32.1	62.9	28.3	15.0
2007gi	6.7	$3.6 - 9.2$	20.4	11.1	32.9	4.0
2007on	49.7	$1.7 - 416.6$	28	108.1	36.1	13.2
2007S	64.4	$7.6 - 312.7$	60	83.7	83.2	19.6
2007sr	30.6	$2.7 - 192.1$	28	92.4	12.7	5.3
2008A	53.5	$5.6 - 318.4$	70	51	89.5	18.5
2008ae	9.26	$2.7 - 873.5$	127	18.8	434	16.9
2008dx	5.4	$3.9 - 7.1$	97	5.4	2328.2	29.8
2008ge	23.2	$14.7 - 28.8$	16	8.3	19.3	5.6
2008ha	36.4	$4.3 - 88.0$	22.5	11	26.8	8.3
2008hs	25.9	$2.0 - 58.6$	74.2	68	123.2	15.1
2008hv	89.4	$2.7 - 60.3$	48.8	63.5	28.2	13.4
2008Q	78.9	$5.0 - 494.1$	32	64.2	16	9.5
2009an	10.9	$4.3 - 25.8$	39.9	60.7	27.6	4.6
2009cz	24.3	$8.7 - 433.8$	90	72.9	93.7	12.7
2009dc	29.5	$16.5 - 54.2$	89.3	28.8	198.9	20.5
2009gf	26.9	$1.7 - 68.0$	75.8	70	46.4	9.4
2009ig	16.3	$1.8 - 53.4$	36.7	132	14.2	4.1

Table 1 (continued): Type Ia Supernova Properties

Supernova	Weighted Average Date [days after discovery]	Date Range	Distance [Mpc]	Exposure Time [ks]	Luminosity (0.2-10 keV) 3σ upper limit [10^{38} erg s^{-1}]	Mass Loss Rate 3σ upper limit [$\frac{10^{-6}\mathrm{M_\odot yr^{-1}}}{10\mathrm{kms^{-1}}}$]
2009ig	16.3	$1.8 - 53.4$	36.7	132	14.2	4.1
2009iz	5.2	$3.7 - 8.0$	55	11.5	160.4	7.7
2009jr	12.4	$7.7 - 17.4$	64	18.8	227.3	14.2
2009Y	16.5	$4.8 - 55.4$	123.7	136.9	735.1	29.4
2010ae	17.4	$3.6 - 33.2$	17	11.2	22.5	5.3
2010el	9.5	$4.1 - 15.8$	30.19	6.5	585.4	19.9
2010ev	13.6	$3.9 - 32.2$	32.25	75.7	38.2	6.1
2010fy	7.7	$3.7 - 11.5$	50	10.7	180.7	10.0
2010gp	33.6	$10.6 - 59.0$	100	49.8	260.7	25.0
2010hh	14.5	$2.1 - 12.2$	80	8.8	408.9	20.6
2010Y	16.8	$1.9 - 36.1$	46	8.1	398.1	21.9
2010ih	16.7	$6.6 - 27.8$	17.05	17.1	19.1	4.8
2010kg	19.9	$4.0 - 36.6$	19.24	43.4	136.8	13.9
2010ko	20.6	$2.0 - 33.3$	10.78	59.8	44.9	8.1
2011B	24.7	$4.7 - 79.0$	25.5	74.7	13.1	4.8
2011M	13.2	$6.6 - 20.0$	13.38	35.3	349.6	18.1
2011aa	26.7	$5.6 - 59.6$	25.35	56.1	52.4	10.0
2011ao	16.8		36.8	93.0	17.1	4.5

3.2 Method

We co-added all individual observations (ObsIDs) using the *ximage* software package (version 4.4.1) to produce a sky image for each supernova. We then used the *ximage* analysis package to determine a 3σ upper limit on count rate for each supernova image, using a 5 pixel radius corresponding to point spread function encircled energy radius of roughly 90% centered on the optical position of the respective supernova and a background region in a source-free region of the image. These count rates were corrected for 100% encircled energy radius and were converted to an unabsorbed flux using the online *pimms* tool (version 4.3) using the appropriate column density for the host galaxy [Dickey & Lockman(1990)] and assuming a 10 keV thermal bremsstrahlung plasma [Fransson et al.(1996)]. By making the assumption that all SNe Ia result from the same type of progenitor system, we can follow [Panagia et al.(2006)] to add these 53 upper limits using the equation: $\sigma^2 = \left(\Sigma_i \sigma_i^{-2}\right)^{-1}$, where σ_i is the upper limit from the i-th supernova and we sum over all of the SNe in our sample. We combine the individual images centered on the SN location to produce a stacked image, shown in Figure 3.1.

In order to determine the rate of material lost by Type Ia supernova systems via the winds of a possible companion star, we make several assumptions with respect to model and parameters. We assume spherically symmetric stellar wind, and we calculate the mass loss rate via [Chevalier & Fransson(2003), Immler et al.(2006)]:

$$L = \frac{1}{4\pi m^2}\Lambda(T)\left(\frac{\dot{M}}{v_w}\right)^2 (v_s t)^{-1} \qquad (3.1)$$

15
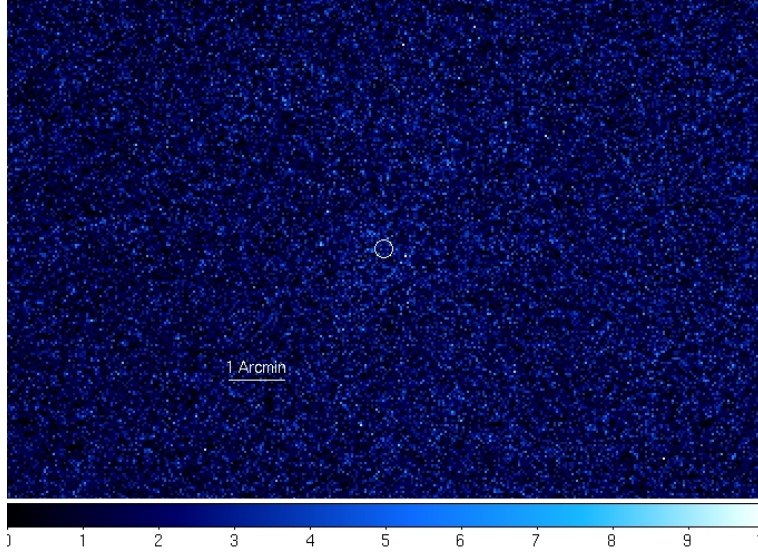
Figure 3.1: Stacked image of all Type Ia supernovae included in this sample.

where L_x is the X-ray luminosity determined from the data, m is the average particle mass of 1.8×10^{-27} kg for a H+He plasma with solar composition, t is the time after outburst determined by weighted average, v_s is the shock speed assumed to be 10 000 km s^{-1}, v_w is the wind speed, which for red supergiants ranges from $5 - 25$ km s^{-1}, and here we assume it to be 10 km s^{-1}, and Λ is the cooling function: $\Lambda = 2.4 \times 10^{-27} g_{ff} T_e^{1/2}$, where T_e is the electron temperature ($T_e = 1.36 \times 10^9 (n-2)^{-2} \left(\frac{v_s}{10^4 kms^{-1}}\right)^2$ K) and g_{ff} is the free-free Gaunt factor. n is the power law index of the SN ejecta: $\rho \propto r^{-n}$ and ranges from 7 - 10. Here we assume it to be 8. The reverse shock is in equipartion unless $T > 5 \times 10^8$ K [Chevalier & Fransson(2003)].

Using the same images, all sources were removed with the detect/remove command in ximage. These 'cleaned' images were then analyzed in the same way as above, and results were similar.
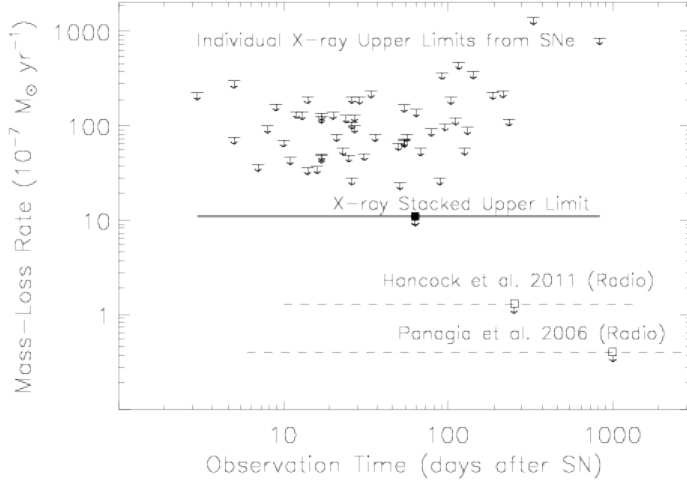
Figure 3.2: Recent results for mass-loss rate upper limits, including the results from this study and those of [Panagia et al.(2006)] and [Hancock et al.(2011)] (both in radio).

3.3 Results

None of the 53 SNe Ia are detected at any time or in stacked images. For the individual SNe, we find the X-ray luminosity 3σ upper limits range from 2.7×10^{38} erg s^{-1} to 2.3×10^{41} erg s^{-1} (0.2-10 keV). The mass-loss rate upper limits range from 7.5×10^{-5} to 4.0×10^{-6} M$_\odot$ yr^{-1} $\times (v_{\rm w})/(10$ km s^{-1}). By analyzing the stacked image, we obtain a 3σ upper limit on the X-ray Luminosity of 1.7×10^{38} erg s^{-1} and a 3σ upper limit on the mass loss rate of 1.1×10^{-6} M$_\odot$ yr^{-1} $\times (v_{\rm w})/(10$ km s^{-1}). All luminosities are reported in the 0.2-10 keV energy band.

3.4 Discussion

In this paper we present the deepest flux limits and upper limits on the mass-loss rates of SNe Ia companion objects obtained from X-ray observations to date. These results are combined with those obtained at radio wavelengths of other studies in Figure 3.2. From these mass-loss upper limits, we can make statements about the progenitor system for a generic, average SN Ia, assuming that SNe Ia form a homogeneous class of objects.

Radio and X-ray studies of nearby core-collapse SNe have shown that the mass-loss rates of massive progenitors are well above the limit inferred in this study (10^{-6} –10^{-5} $M_\odot$ yr^{-1}). Wind accretion is generally about 10% efficient [Yungelson et al.(1995)]. If 10% of the wind is being accreted onto the white dwarf, that would increase the mass loss from the companion by 10% over the upper limits presented here. The result is still below the mass-loss expected from a massive star, and therefore we can rule out wind from a massive star accreting onto a white dwarf as the progenitor system for SNe Ia. We cannot rule out a main sequence star as a companion with mass-loss rates $< 10^{-7}$ $M_\odot$ yr^{-1} in a wind-accretion scenario. A double-degenerate white dwarf system is also not excluded due to the lack of CSM interaction and hence the lack of emitted X-rays. The possibility of a massive companion in Roche Lobe overflow is also still permitted by these limits. Our results qualitatively support results from other wavelength regimes, such as in the radio [Panagia et al.(2006),Hancock et al.(2011)] and in the UV [Brown(2011)].

Our results improve on the previous lowest published upper limit derived from

X-ray observations, 3×10^{-6} M$_\odot$ yr^{-1} v_w/(10 km s^{-1}) from [Immler et al.(2006)]. This new limit is about 1/3 that of theirs.

Since the X-ray emission from Type Ia Supernovae results from a different process than radio emission and from different regions in the shocked circumstellar medium, these results provide a completely independent check on the results of others.

The mass-loss rate is sensitive to both time after outburst of observation and distance of the supernova. Therefore, it is possible for individual SNe to give similar or even lower upper limits than the stacked data; the stacked data, however, give results for the entire sample as a whole. These results give upper limits for a homogeneous class of objects, but it is not certain whether all SNe Ia have the same progenitor systems.

Several of the observations included in this study have been of SNe at very early times (for example, SN 2005bc was observed at 2.7 days after discovery of the SN), when the X-ray emission would be highest due to the higher CSM density found at smaller radii. For these early observations, the upper limit we derive for the mass-loss rate is on the order of 10^{-5} M$_\odot$ yr^{-1} v_w/10 km s^{-1}. The X-ray luminosity upper limits are on the order of 10^{41} erg s^{-1}.

Further early and sensitive observations are still needed to address questions about the nature of SNe Ia progenitor systems. Prompt X-ray observations during or shortly after the explosion will enable us to probe the circumstellar environment down to the surface of the white dwarf, allowing us to further constrain the properties of the companion star.

3.5 Summary

Using the largest sample of SNe Ia available for stacking analysis, we have generated a deep *Swift* XRT X-ray image of 3.05 Ms exposure time. We determine that there is no X-ray source at the position of the stacked SNe. We calculate a 3σ upper limit for the X-ray luminosity of 1.7×10^{38} erg s^{-1}, and an upper limit on the mass-loss rate of 1.1×10^{-6} M$_\odot$ yr$^{-1} \times (v_{\mathrm{w}})/(10$ km s$^{-1})$ from the SN progenitors. The low upper limits provide further evidence that the companion stars in SNe Ia progenitor systems are not a massive star (e.g. red supergiant or post main-sequence) in a wind-accretion scenario. Lower-mass main sequence stars with small amounts of mass lost in stellar winds, a white dwarf companion in double-degenerate SNe Ia systems, or a massive star in Roche lobe overflow are not excluded. It is also possible that SNe Ia do not form a homogeneous class of objects, in which case there may be individual detections of X-rays from some SNe Ia.

Chapter 4: Clusters of Galaxies – Introduction

Clusters of galaxies consist of a large number of galaxies, and are the largest systems bound by gravity in the Universe ([Jones et al.(2008)]). They also contain tenuous gravitationally-bound gas between the galaxies ([Sarazin(2008)]). This gas, known as the Intracluster Medium (ICM), exists at very high temperatures generated from falling into the gravity well and being thermalized by shocks ([Jones et al.(2008)]), and comprises more mass in the cluster than do the galaxies ([Sarazin(2008)]). It has temperatures of approximately 10^7 K and emits X-rays. Also present is a dark matter halo, that comprises most of the mass of the cluster ([Sarazin(2008)]). Only approximately 15% of the matter in clusters is non-dark matter, and of that, up to 80% is found in the hot ICM ([Jones et al.(2008)]). Additional heating of the gas may be provided by Active Galactic Nuclei present in the clusters, which may accrete matter from cooling gas then release it in outbursts ([Jones et al.(2008)]).

Clusters of galaxies are also significant in cosmological studies [Sunyaev(1971)], [Press & Schechter(1974)], [White et al.(1993)]. However, the thermal conductivity in clusters is unknown. The thermal conductivity is very important in understanding the physics of what occurs in the cool cores and at the cluster outskirts.

The primary X-ray emission method for the gas at this temperature is thermal bremsstrahlung, also with line emission ([Jones et al.(2008)]). This allows the ICM gas density profiles to be determined with observations of the X-ray surface brightness, and the temperature profile and abundances are calculated based on spectroscopy ([Jones et al.(2008)]). Since the gas is generally in hydrostatic equilibrium ([Sarazin(2008)] and [Sarazin(1988)]), we have:

$$\frac{1}{\rho_g}\frac{dP}{dr} = -\frac{GM(r)}{r^2} \tag{4.1}$$

(where ρ_g is the gas density, G is the gravitational constant, $M(r)$ is the mass contained within radius r, and $P = \rho_g kT_g/\mu m_p$), the total mass profile of the cluster can be determined observationally as well [Jones et al.(2008)]. This total mass profile generally agrees with the Navarro-Frenk-White [Navarro et al.(1996)] profile [Jones et al.(2008)]:

$$\rho_{tot} \propto \left(\frac{r}{r_s}\right)^{-1}\left(1 + \frac{r}{r_s}\right)^{-2} \tag{4.2}$$

where r_s is the scale radius, calculated by $r_s = \frac{c_{500}}{r_{500}}$ [Vikhlinin et al.(2006)]. r_{500} is the radius at which the density of the total mass in the cluster is 500 times the critical density and c_{500} is the concentration parameter as determined by [Vikhlinin et al.(2006)].

Given that the ICM possesses temperature gradients, thermal conduction takes places within the gas. Thermal conduction may be described by the standard, full Spitzer conduction equation [Sarazin(1988)]:

$$Q = -\kappa \nabla T \tag{4.3}$$

where Q is the heat flux, T is the temperature, and κ is the thermal conductivity [Spitzer(1958)]:

$$\kappa = 1.31 n_e \Lambda_e k (kT_e/m_e)^{5/2} \tag{4.4}$$

where n_e is the electron number density, $\Lambda = 37.8 + \ln\left[\left(\frac{T_e}{10^8 \mathrm{K}}\right)\left(\frac{n_e}{10^{-3}\mathrm{cm}^{-3}}\right)\right]$ is the Coulomb logarithm (which we set to 40) [Sarazin(1988)].

If we follow a Lagrangian element in the gas, the following conservation of energy equation will hold [Sarazin(1988)]

$$\frac{3}{2}\frac{\rho_g k}{\mu m_p}\frac{dT_g}{dt} - \frac{kT_g}{\mu m_p}\frac{d\rho_g}{dt} = -\nabla \cdot \mathbf{Q} \tag{4.5}$$

This equation doesnt include radiative cooling, which we will discuss below.

However, the presence of tangled magnetic field lines within the cluster [Feretti & Giovannini(2008)], [Carilli & Taylor(2002)] may prevent full Spitzer conduction, as the conduction is due primarily to electrons [Sarazin(2008)]. Because the electron gyro-radius for the fields expected in these clusters ($\approx 1 - 10\mu$G [Carilli & Taylor(2002)]) is much smaller than the Coulomb mean free path, conduction occurs primarily along magnetic field lines. Therefore, the effective thermal conductivity is determined by the field, and will be reduced from the Spitzer value (Eq 4.4). For a randomly tangled magnetic field, this suppression factor is expected to be on the order of 3 [Sarazin(1988)], [Gruzinov(2002)]. There are also special

regions of magnetic fields, for example in cold fronts where thermal conduction is strongly suppressed [Markevitch, et al.(2000)], [Ettori & Fabian(2000)], [Vikhlinin et al.(2001)], [Markevitch & Vikhlinin(2007)]. It is the goal of this part of the thesis to use computational modelling to constrain the conductivity suppression factor.

The gas also experiences radiative cooling due to thermal bremsstrahlung radiation, with emissivity [Sarazin(1988)]:

$$\epsilon^{ff} = 3.0 \times 10^{-27} T_g^{1/2} n_p^2 \text{erg cm}^{-3}\text{s}^{-1} \tag{4.6}$$

This equation is valid when the gas temperatures are above 3×10^7 K, which is valid in the clusters we study here.

Note that this cooling is significantly more pronounced at high densities, and therefore is a major contributor to the temperature change only near the central portion of the cluster. As the gas there cools, it also compresses as a result of the pressure from the outer parts of the gas in order to maintain hydrostatic equilibrium [Sarazin(2008)].

Many clusters are observed with a significant peak in the X-ray brightness profile at the center of the cluster [Jones et al.(2008)]. This indicates that high-density gas exists in this region, which lowers the cooling time of the gas to much less than the age of the cluster [Jones et al.(2008)]. In fact, cooler gas is observed in the central region [Jones et al.(2008)], but the expected cooling catastrophe, in which the gas cools and flows into the central galaxy, is not observed [Jones et al.(2008)]. The reheating of the gas may be due to cluster mergers or thermal conduction, or

more likely due to AGN feedback mechanisms and sloshing [Jones et al.(2008)].

Clusters undergo mergers with other clusters. This disrupts the temperatures and gas density profiles significantly. Between these merger episodes, clusters tend to relax. It takes on the order of 1 Gyr for a cluster to relax following a merger, and mergers occur on the order of approximately 5 Gyr between mergers.

The temperature and density profiles of symmetric, relaxed clusters are similar [Markevitch(1998)], [Vikhlinin et al.(2005)] outside of the cluster core (where cooling plays a major role, and AGN feedback is relevant also [Jones et al.(2008)]).

Over time, due to thermal conduction and the resultant redistribution of the gas to maintain hydrostatic equilibrium, the gas fraction (defined as the ratio of the gas density to the total mass density) will change with time, as will the temperature profile. This is precisely what we model in this paper.

[Vikhlinin et al.(2005)] and [Vikhlinin et al.(2006)] have studied a series of clusters and fit the gas temperature and density profiles to a model with a number of free parameters. The gas temperature was fit to a 3-dimensional model:

$$T_{gas} = T_0 \frac{(r/r_{cool})^{a_{cool}} + T_{min}/T_0}{(r/r_{cool})^{a_{cool}} + 1} \frac{(r/r_t)^{-a}}{\left[1 + (r/r_t)^b\right]^{b/c}} \tag{4.7}$$

r is the radius, and the remaining symbols are parameters in their fit. In this work, we use the temperature profiles as fit by Vikhlinin as the initial profiles for the clusters we study. They also fit the gas density profile to:

$$n_p n_e = n_0^2 \frac{(r/r_c)^{-\alpha}}{(1 + r^2/r_c^2)^{3\beta - alpha/2}} \frac{1}{(1 + r^\gamma/r_s^\gamma)^{\epsilon/\gamma}} + \frac{n_{02}^2}{(1 + r^2/r_{c2}^2)^{3\beta_2}} \tag{4.8}$$

25

The Vikhlinin study included a number of clusters with a range of temperatures. In this study, we choose clusters A478 (peak temperature 9 keV), A907 (7 keV), A1413 (8 keV), A1795 (7 keV), and A2029 (9 keV) to include a range of cluster temperatures, and to include clusters with and without an initial cool core (a region of lower temperature at the cluster center).

[Mantz et al.(2014)] have analyzed the gas density profiles for 40 massive, dynamically relaxed clusters and have determined the intrinsic scatter in the gas fraction between these clusters as a function of radius (in terms of r_{2500}, the radius at which the density is 2500 times the critical density). They find an intrinsic scatter ranging between 7 % and 12 %.

In order to constrain the thermal conduction suppression factor, we have run a grid of simulations. For each cluster we study, we simulate the thermal conduction and gas redistribution for a range of thermal conduction factors, from 0.05 of the full Spitzer value to 0.5 of the Spitzer value, for a time of 8 Gyr. This results in time-changing temperature and gas fraction profiles. We are able to compare our results for each cluster around r_{2500} to the results of [Mantz et al.(2014)].

Chapter 5:   Clusters – Methods

We model the behavior of the Intracluster Medium (ICM) over a period ranging from 0 - 8 Gyr for five clusters: A478, A907, A1413, A1795, A2029. These were chosen to include a range of peak gas temperature and to include both clusters with and without an initial cool core. These clusters are also in the same range of average temperatures of the sample of [Mantz et al.(2014)]. We simulate the evolution of the temperature and gas density profiles with a series of thermal conduction suppression factors, ranging from 5% to 50% of full Spitzer conduction.

5.1   Initial Conditions

We begin by fitting projected temperature profiles from a cluster to the three-dimensional model from [Vikhlinin et al.(2006)]: Eq 4.7 We also take a Navarro-Frenk-White total mass profile (Eq 4.2) [Navarro et al.(1996)], using parameters as fit by [Vikhlinin et al.(2006)]. This is scaled to produce the observed total cluster mass at r_{500}, as given in Table 5.1.

From these two profiles, we assume that the gas is in hydrostatic equilibrium (Eq 4.1), and use this to calculate the gas density from the Vikhlinin temperature profile and the NFW mass profile, scaling the density in such a way that the density

Table 2: Initial Cluster Total Mass Profile Parameters

Cluster	r_{500}	c_{500}	M_{500}	$f_{g,500}$
			10^{14} M$_\odot$	
A478	1337	3.57	7.68	0.120
A907	1096	3.48	4.56	0.124
A1413	1299	2.93	7.57	0.107
A1795	1235	3.21	6.03	0.104
A2029	1362	4.04	8.01	0.123

at r_{500} matches the value obtained in Vikhlinin.

We follow the gas in Lagrangian bins initially placed evenly through the cluster. The central bin is treated as a spherical shell with an inner boundary of 10 kpc. We choose this limit to avoid modeling the central part of the cluster. The number of bins is set to 2000, and results are discussed in Chapter 6.

Tables 2 and 3 give the parameters of the initial conditions (from [Vikhlinin et al.(2005)] and [Vikhlinin et al.(2006)]), and Figures 5.1 through 5.10 show the initial gas temperature and gas density profiles for each cluster.

5.2 Thermal Conduction

The thermal conduction is incorporated in the following way. We fit the temperature profile to the Vikhlinin form 4.7 at each time step.

This fit is accomplished using a simulated annealing chi-square fit to the data,

Table 3: Initial Cluster Temperature Profile Parameters

Cluster	T average, excluding core	T peak T_0	r_t	a	b	c	
	keV	keV	kpc				
A478	7.9	9	11.06	0.27	0.02	5.0	0.4
A907	5.9	7	10.19	0.24	0.16	5.0	0.4
A1413	7.3	8	7.58	1.84	0.08	4.68	10.0
A1795	6.1	7	9.68	0.55	0.00	1.63	0.9
A2029	8.5	9	16.19	3.04	-0.03	1.57	5.9

Table 3 (continued): Initial Cluster Temperature Profile Parameters

Cluster	T_{min}/T_0	r_{cool}	a_{cool}
		kpc	
A478	0.38	129	1.6
A907	0.32	208	1.48
A1413	0.23	30	0.75
A1795	0.10	77	1.03
A2029	0.10	93	0.48
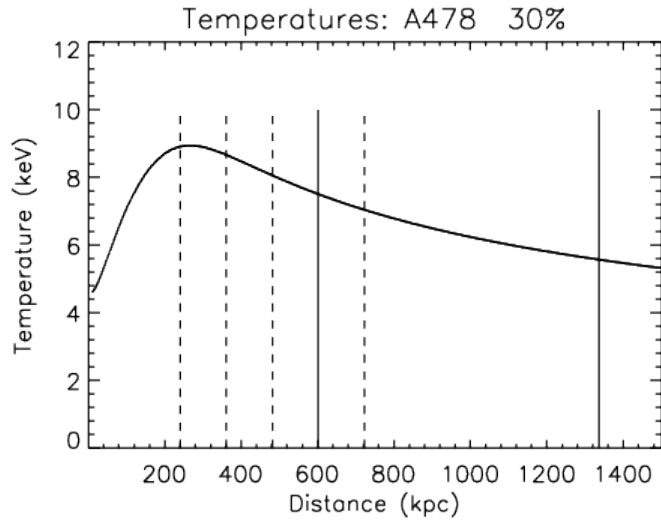
Figure 5.1: Initial Gas Temperature Profile for A478
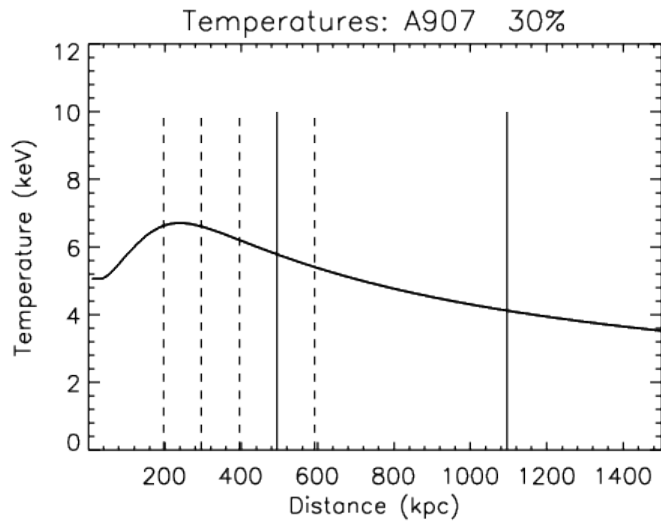
Figure 5.2: Initial Gas Temperature Profile for A907
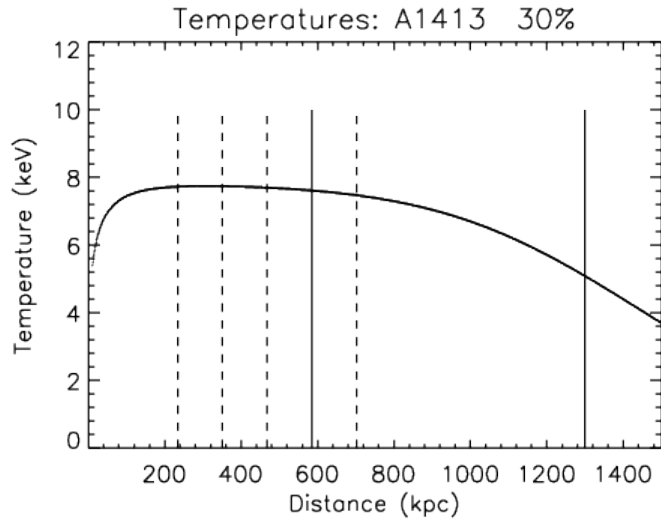
Figure 5.3: Initial Gas Temperature Profile for A1413
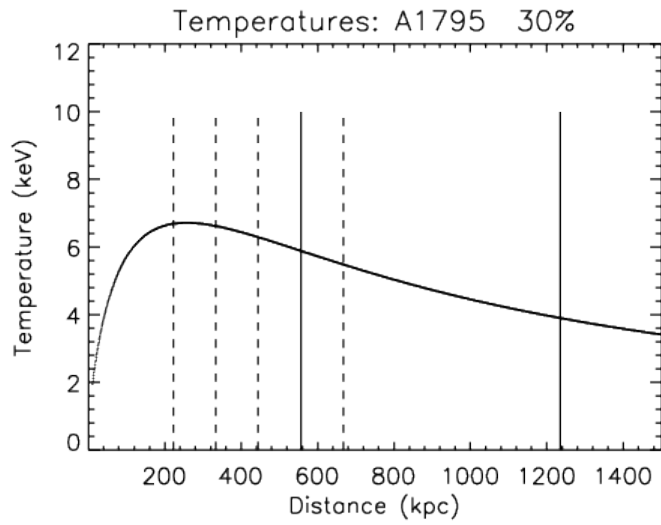
Figure 5.4: Initial Gas Temperature Profile for A1795
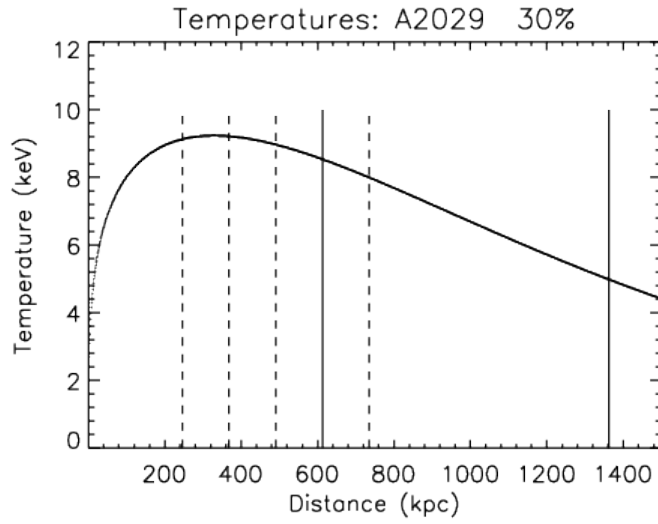
Figure 5.5: Initial Gas Temperature Profile for A2029
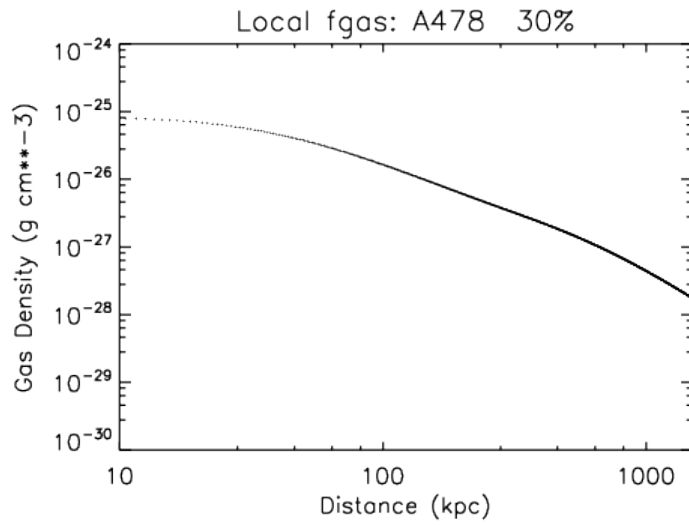
Figure 5.6: Initial Gas Density Profile for A478
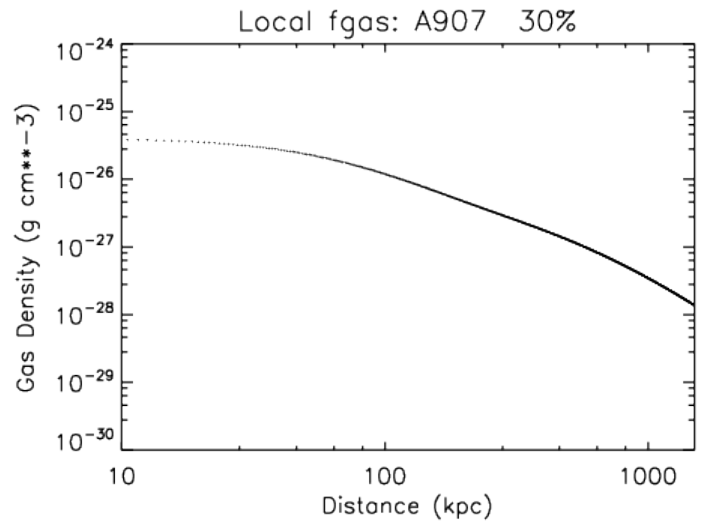
Figure 5.7: Initial Gas Density Profile for A907
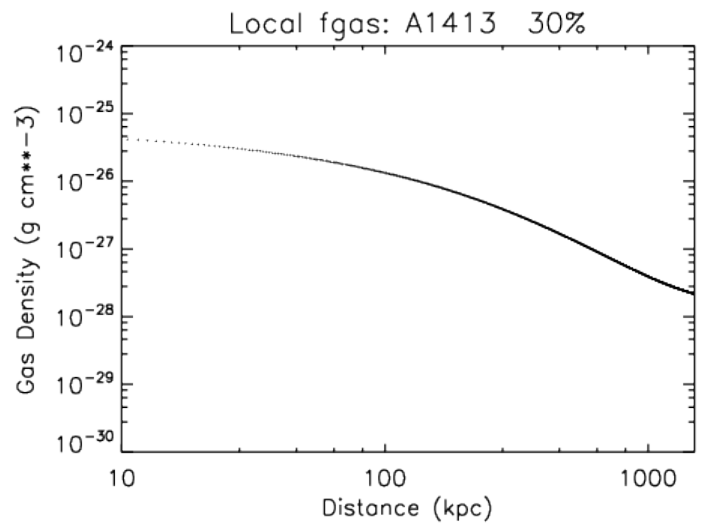
Figure 5.8: Initial Gas Density Profile for A1413
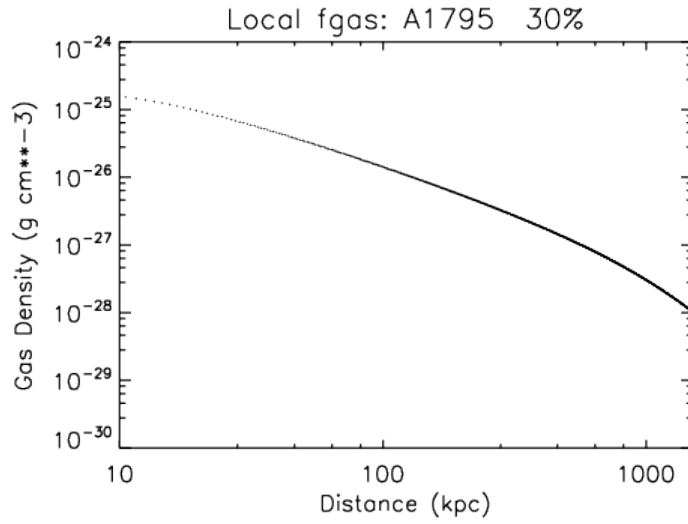
Figure 5.9: Initial Gas Density Profile for A1795
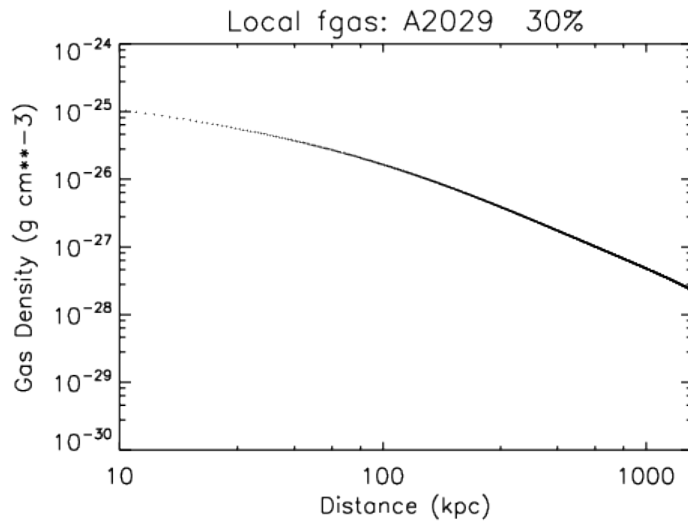
Figure 5.10: Initial Gas Density Profile for A2029

and is rejected if the discrepancy between the fit and the temperature at any point is greater than both 3% and 0.01 keV, except at the center during the cool core phase describe below. From this fit, we calculate the first two spatial derivatives of the temperature profile. This method is used to minimize numerical errors associated with the limited number of spatial bins. The thermal conduction is given by the heat flux [Sarazin(1988)] 4.3

In this work, we run simulations with the conductivity ranging from 0.05 to 0.5 of the Spitzer value. We set the Coulomb logarithm to 40 for computational simplicity.

We then use the Eq 4.5 to determine the temperature change.

The divergence of Q in spherical symmetry is given by

$$\nabla \cdot \mathbf{Q} = -\kappa(r) \left[\frac{2}{r} \frac{\partial T}{\partial r} + \frac{5}{2} \frac{1}{T(r)} \left(\frac{\partial T}{\partial r} \right)^2 + \frac{\partial^2 T}{\partial r^2} \right] \tag{5.1}$$

assuming spherical symmetry.

We calculate the necessary values, including the first and second derivatives of the temperature profiles, at the center of the appropriate bin, and use equation 4.5 to determine the new temperature. We assume that the change in the gas density is small, and set it to zero here. This results in:

$$\frac{dT}{dt} = -\frac{2}{3} \frac{\mu m_p}{\rho_g k} \nabla \cdot \mathbf{Q} \tag{5.2}$$

With these assumption, we calculate the change in temperature, with initial

time steps of 10^{14} s. This time step is allowed to decrease to keep it below the cooling time limit:

$$t_{cool} = \frac{3}{2} \frac{n_e T}{dT/dt_{cool}}$$ (5.3)

where dT/dt_{cool} is given below (Eq 5.4).

5.3 Cooling

Cooling is included as an additive (or subtractive) term added to dT/dt, from Eq 4.6:

$$\frac{dT}{dt}_{cool} = -\epsilon^{ff}(r)\text{Vol}(r)$$ (5.4)

where $\text{Vol}(r)$ is the volume of the bin at location r. For most of the clusters in this study, the cooling is sufficiently strong at the center to eventually lead to a very pronounced cool core. This would lead to a cooling runaway situation. We account for this by setting a minimum temperature of 0.5 keV. Cooling is gradually reduced as it approaches this level by a factor of $1 - \left(\frac{T_{min}}{T}\right)^2$, to avoid a sudden shutoff. Once a bin reaches this temperature, the cooling is turned off and the bin is removed from the fit (because the form of the fitting function does not allow for such a feature). The effect of the cooling is tested to ensure it doesn't significantly impact the results. This is tested in the Testing section below.

5.4 Gas Redistribution

After determining the new temperature in each bin, we determine whether the cluster is in hydrostatic equilibrium. We rearrange the hydrostatic equilibrium equation Eq 4.1 to:

$$\frac{dP}{dr} = \rho_g \frac{GM(r)}{r^2} \tag{5.5}$$

Converting this equation to refer to the bins we have (subscript i refers to the ith bin), and definining $g_i = -\frac{GM_i}{r_i^2}$, where M and r here are measured at the bin boundary, we get:

$$\left.\frac{\Delta P}{\Delta r}\right|_i = \frac{1}{2} \left(\rho_i + \rho_{i+1}\right) g_i \tag{5.6}$$

$$\frac{P_{i+1} - P_i}{r_{i+1} - r_i} = \frac{1}{2} \left(\rho_i + \rho_{i+1}\right) g_i \tag{5.7}$$

We use this to test whether the gas is in hydrostatic equilibrium, using the following test:

$$\frac{\left| \frac{P_{i+1}-P_i}{r_{i+1}-r_i} - \frac{1}{2} \left(\rho_i + \rho_{i+1}\right) g_i \right|}{\frac{1}{2} \left(\rho_i + \rho_{i+1}\right) g_i} < 10^{-2} \tag{5.8}$$

This is tested at every bin boundary. If the limit is not satisfied for any boundary, we employ an iterative method to allow the gas to relax to hydrostatic equilibrium.

First, we assume that in this stage the thermal conduction can be ignored. Beginning with the boundary between the center-most bin and the adjacent bin, we

adjust the pressure by equal and opposite amounts:

$$P_{new}(i) = P(i) + c\left[P(i+1) - P(i) + g(i)\frac{\rho_g(i+1) + \rho_g(i)}{2}(r(i+1) - r(i))\right]/2$$
(5.9)

$$P_{new}(i+1) = P(i+1) - c\left[P(i+1) - P(i) + g(i)\frac{\rho_g(i+1) + \rho_g(i)}{2}(r(i+1) - r(i))\right]/2$$
(5.10)

where c is a coefficient, set here to 0.5.

We repeat this process at every bin boundary. At the outer edge of the simulation, we simply extrapolate the appropriate values of temperature, density, etc, and treat it as though there were an additional bin just beyond the outer boundary.

Following this process, we adjust the other intrinsic values of the bins. We assume the gas behaves adiabatically, which leads to the volume in bin i changing by:

$$Vol_{new}(i) = Vol(i)\left(\frac{P(i)}{P_{new}(i)}\right)^{3/5}$$
(5.11)

This, in turn, changes the gas density in the bin by:

$$\rho_{g,new}(i) = \rho_g(i)\frac{V(i)}{V_{new}(i)}$$
(5.12)

because we are following Lagrangian bins, the total gas mass in each bin doesn't change. We do assume, however, that the total mass in the cluster (and therefore

g) doesn't change with the gas redistribution.

With a new gas density and pressure in each bin, we are able to calculate a new temperature:

$$T_{new}(i) = \frac{P_{new}(i)\mu m_p}{\rho_{g,new}(i)} \tag{5.13}$$

We also adjust the physical position of the bins, given their new volumes:

$$r_{new}(i) = \left(\frac{3}{4}Vol_{new}(i) + r_{new}(i-1)^3\right)^{1/3} \tag{5.14}$$

The inner boundary is maintained at 10 kpc, and the total mass of the cluster is assumed to be constant.

Following these calculations, the gas is again checked to determine if it is in hydrostatic equilibrium. If not, the process repeats until the condition in Eq 5.8 is satisfied.

Once the gas is in hydrostatic equilibrium, the new temperature profile is fit to the Vikhlinin profile (Eq 4.7), and the entire process begins again with thermal conduction.

5.5 Tests

In order to ensure that the results of the simulation make physical sense, we conducted several sanity checks. The first was to run the simulation with cooling turned off and without redistribution to ensure that the cluster behaves as expected. The results of this test for cluster A2029 are given in Figure 5.11. Note that the
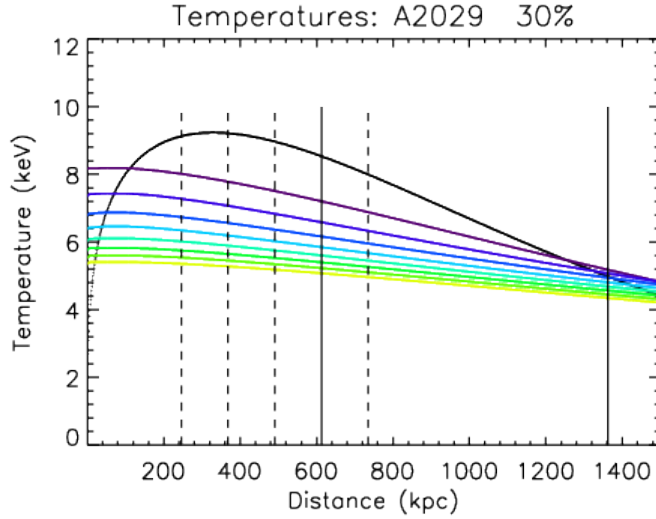
Figure 5.11: Temperature profiles, in 1 Gyr increments, for A2029 without cooling and without redistribution. The black curve represents the initial profile.

cluster becomes nearly isothermal eventually. We then turned on redistribution (but without cooling; Figures 5.12 and 5.13). In this case, the redistribution acts to slow down the effects of the thermal conduction, as expected. The next step was to turn on the cooling (Figures 5.14 and 5.15), which can be compared with the previous results. In this case, the core eventually cools, which is the expected behavior.

Note that outside a radius of approximately 500 kpc, the gas fraction is identical in both cases. This test was completed for each cluster studied. Further results are presented in Chapter 6.

Also note that the temperature profile behaves as expected. The cooler region at the center of the cluster warms, the peak decreases in temeprature, and the tail of the profile increases slightly in temperature. The eventual decrease in temperature across the profile is due to energy leaving the outer bin to the region in which the
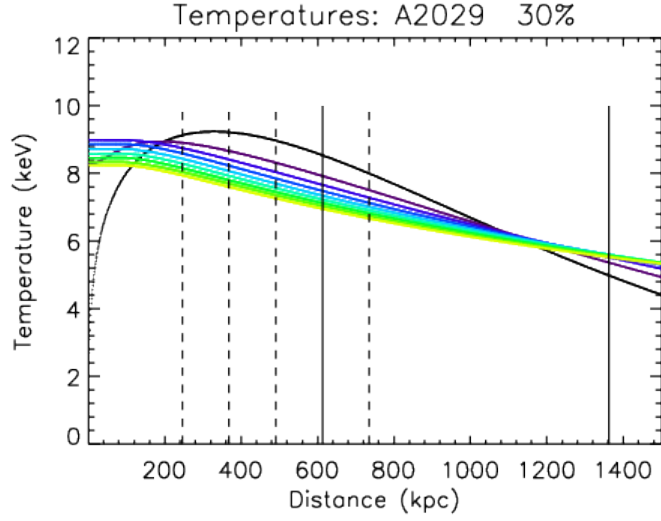
Figure 5.12: Temperature profiles, in 1 Gyr increments, for A2029 without cooling. The black curve represents the initial profile.
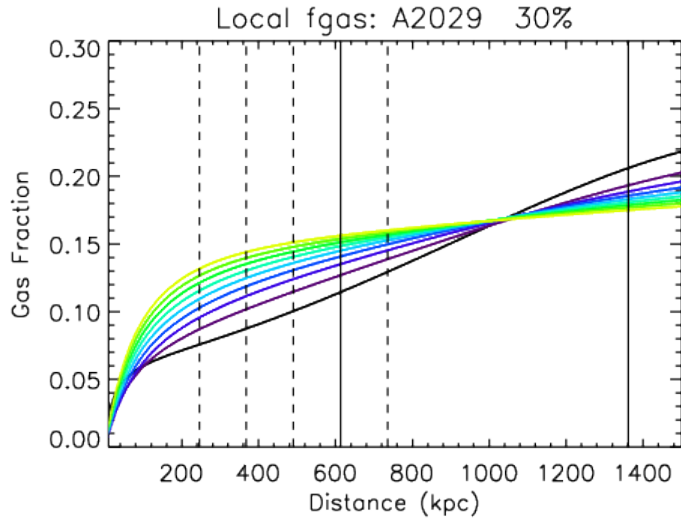
Figure 5.13: Gas density profiles, in 1 Gyr increments, for A2029 without cooling. The black curve represents the initial profile.
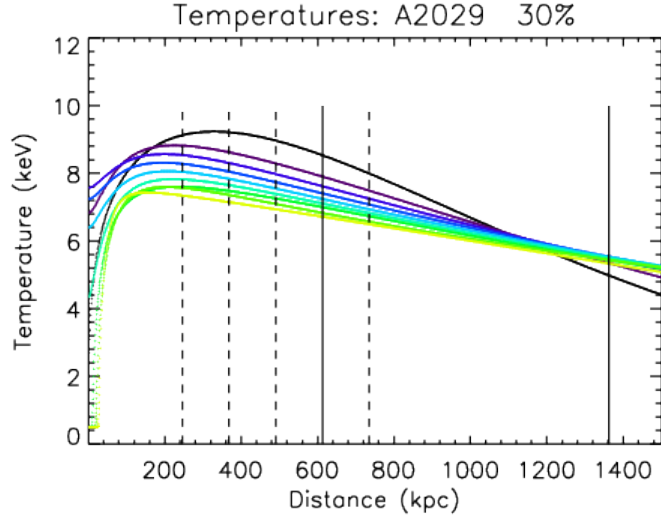
Figure 5.14: Temperature profiles, in 1 Gyr increments, for A2029 with cooling. The black curve represents the initial profile.
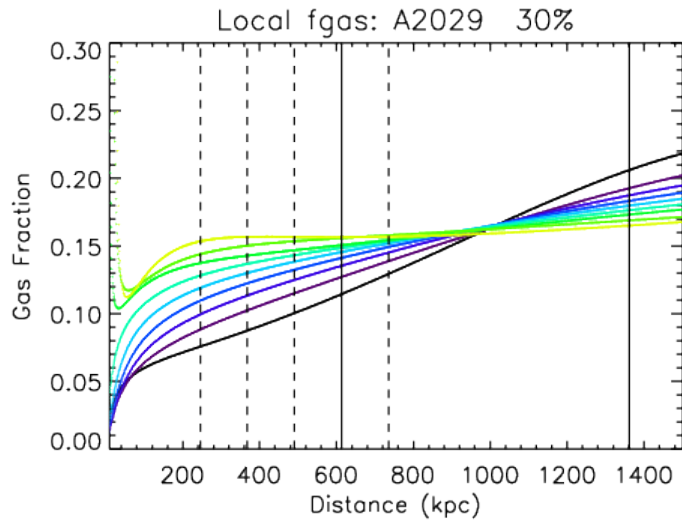
Figure 5.15: Gas density profiles, in 1 Gyr increments, for A2029 with cooling. The black curve represents the initial profile.
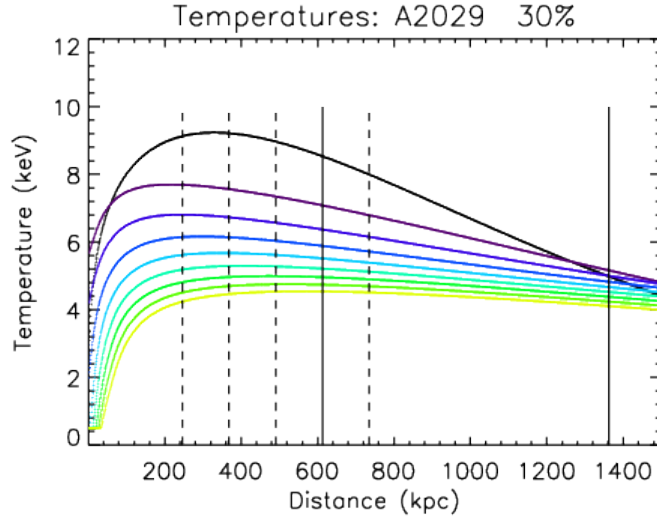
Figure 5.16: Temperature profiles, in 1 Gyr increments, for A2029 with cooling but without redistribution of the gas. The black curve represents the initial profile.

profiles are extrapolated.

We also compare results with and without gas redistribution. These results are shown in Figure 5.16.

In order to ensure that the simplifications we have made do not result in unphysical results, we have compared our results for one case with the results of a fully numerical FLASH simulation, as updated by John ZuHone. We matched initial conditions, boundary conditions, and the cooling function for both simulations. For the case of A2029 with 30% of full Spitzer conduction, the results of the FLASH code and the results of our model are nearly identical.

In order to ensure that the simplifications we have made do not result in un-physical results, we have compared our results for one case with the results of a more complex model, the FLASH model as updated by John ZuHone. We matched
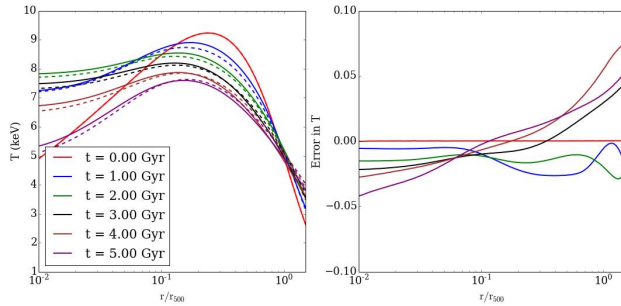
Figure 5.17: Comparison of the results of this simulation (solid) and the results of the more complex FLASH simulation (dashed), for the case of A2029 with 30% of full Spitzer conduction, including radiative cooling. The temperature profiles are printed in 1 Gyr increments, with the initial profile in black.

initial conditions, boundary conditions, and the cooling function for both simulations. For the case of A2029 with 30% of full Spitzer conduction, the results of the FLASH code and the results of our simplified code agree to within a few percent. The relevant results in the region of interest are indistinguishable. See Figures 5.5 and 5.5.

5.6 Science

The goal of this study is to find a constraint on the conduction in hot, relaxed clusters of galaxies. In order to do this, we take as our initial values current observations of cluster temperature profiles. We then evolve them over a period of 8 Gyr to determine how the gas fraction evolves with time as a result of thermal conduction. As noted in Chapter 4, the temperature profiles of hot, relaxed clusters are similar when scaled by the average temperature and when the radius is scaled
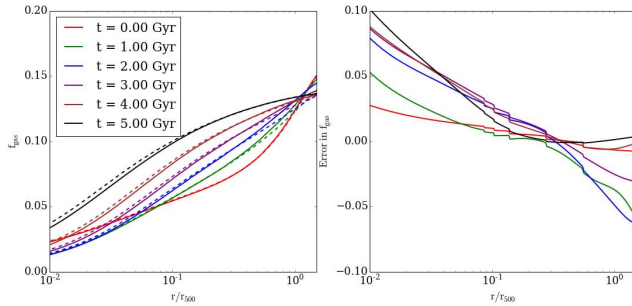
Figure 5.18: Comparison of the results of this simulation (solid) and the results of the more complex FLASH simulation (dashed), for the case of A2029 with 30% of full Spitzer conduction, including radiative cooling. The gas density profiles are printed in 1 Gyr increments, with the initial profile in black.

by the radius of a fixed overdensity.

In order to make conclusions about the results of the simulation, we compare our results to those of [Mantz et al.(2014)]. In particular, we calculate the gas fraction in large bins of 0.4 - 0.8 of r_{2500} and 0.8 - 1.2 of r_{2500}. This is done by integrating the gas density in that region to obtain the gas mass in each bin, then by doing the same with the total mass, and by dividing the two. We next determine the percent change in these larger bins from initial in 1 Gyr increments. This correlates with the scatter reported in [Mantz et al.(2014)] Figure 3 (left panel), which we show in the results section. We compare the percent change we calculate in the first several Gyr with those of [Mantz et al.(2014)]. We note that [Mantz et al.(2014)] select hot, relaxed clusters with temperatures > 5 keV. It is likely that this sample contains clusters of a variety of ages. It takes on the order of 1 Gyr for a cluster to relax from a merger, and mergers happen on the order of 5 Gyr. Therefore, we

assume a scatter in cluster ages of 3 - 5 Gyr. In our analysis, we take initial profiles for clusters as currently observed, and evolve them over time for several Gyr to simulate the resultant scatter in gas fraction. That is, we compare the gas fraction in a cluster at various times. From this, we are able to determine the scatter in gas fraction present assuming clusters have a scatter in age of approximately 3 - 5 Gyr. We are then able to place qualitative limits on the amount of conduction in these hot, relaxed clusters. For ease of comparison, in Chapter 6, we overplot the results of [Mantz et al.(2014)] in the relevant plots.

We have chosen a sample that includes cluster of varying temperatures (from 6 keV to 8.5 keV) to include several temperatures within the sample analyzed by [Mantz et al.(2014)]. We also choose a range of temperatures because conduction scales with $T^{5/2}$.

Chapter 6:   Clusters – Results

We have run the simulation in the grid as described in Chapter 5. Here we present the results with discussion, by cluster arranged by peak temperature.

6.1   A478

Cluster A478, as shown in Chapter 5, has a cool core and has a peak temperature of 9 keV and average temperature outside of the cluster core of 7.9 keV. The grid of plots are shown in Figures 6.1 to 6.14.

6.1.1   Temperature profiles

One thing that stands out immediately is that when the thermal conduction is low (5%, for example), the cooling dominates at the core and the gas there cools rapidly to the lower limit. However, with higher values of conduction, the gas at the core initially warms. When the gradient of the temperature profile becomes small, however, conduction weakens and cooling can dominate once again. Even when conduction is at 50% of full Spitzer, the gas at the core eventually cools to the 0.5 keV limit. Note that the cooling process acts as a feedback loop. As the gas cools, in order to remain in hydrostatic equilibrium, it must compress (so that pressure
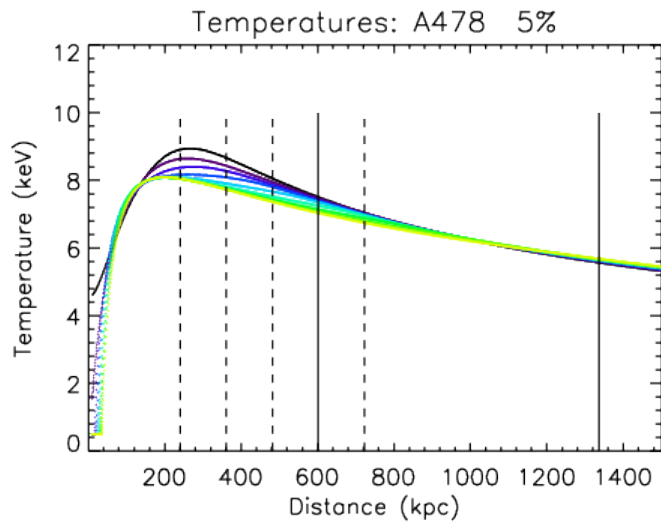
Figure 6.1: Temperature profiles, in 1 Gyr increments, for A478 with a thermal conduction factor of 5%. The black curve represents the initial profile. Solid vertical lines are plotted at r_{2500} and r_{500}, and dashed lines are plotted at 0.4, 0.6, 0.8, and 1.2 of r_{2500}.
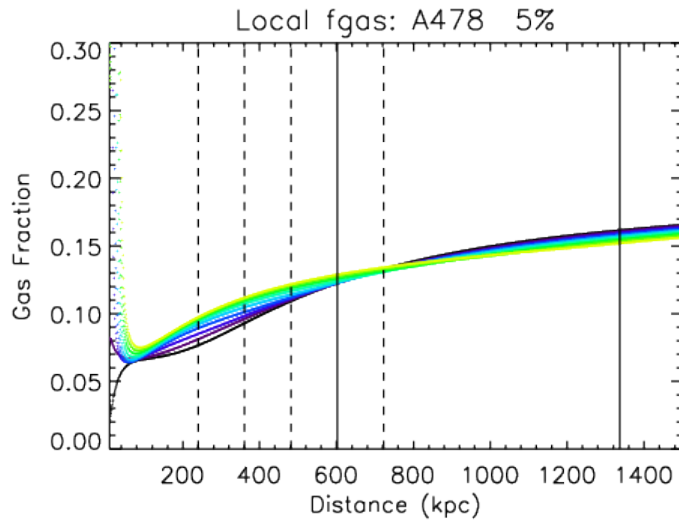
Figure 6.2: Gas fraction profiles, in 1 Gyr increments, for A478 with a thermal conduction factor of 5%. The black curve represents the initial profile. Solid vertical lines are plotted at r_{2500} and r_{500}, and dashed lines are plotted at 0.4, 0.6, 0.8, and 1.2 of r_{2500}.
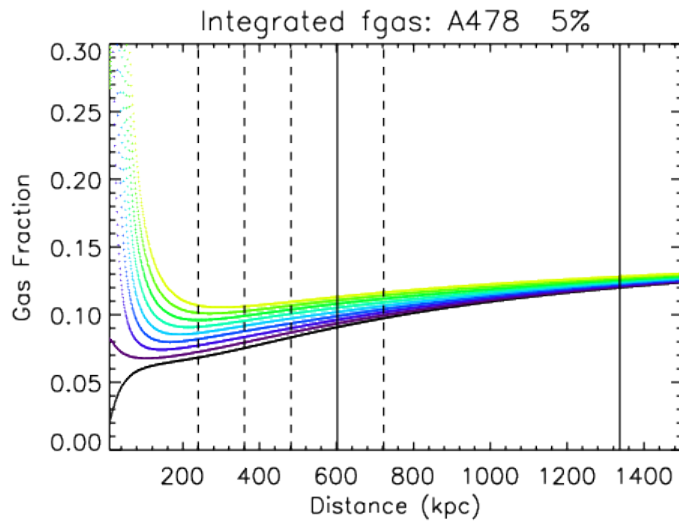
Figure 6.3: Integrated gas fraction profiles, in 1 Gyr increments, for A478 with a thermal conduction factor of 5%. The black curve represents the initial profile. Solid vertical lines are plotted at r_{2500} and r_{500}, and dashed lines are plotted at 0.4, 0.6, 0.8, and 1.2 of r_{2500}.
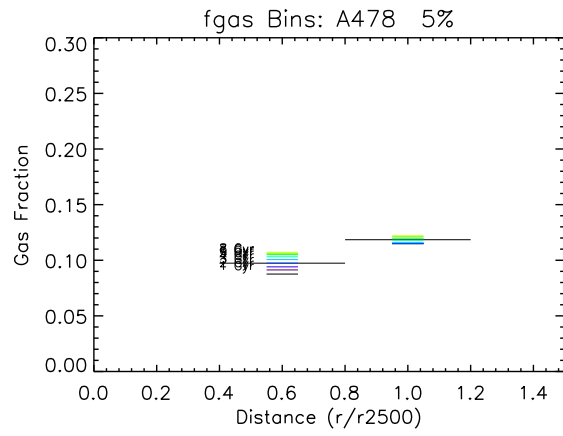
Figure 6.4: Binned gas fraction, in 1 Gyr increments, for A478 with a thermal conduction factor of 5%, plotted as a function of r/r_{2500}.
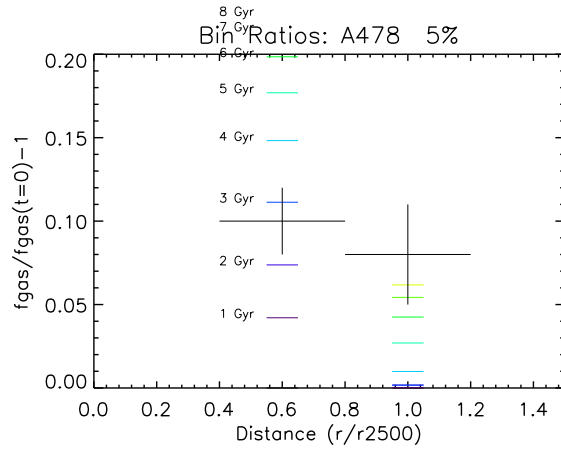
Figure 6.5: Fractional change in binned gas fraction, in 1 Gyr increments, for A478 with a thermal conduction factor of 5%, plotted as a function of r/r_{2500}. The intrinsic scatter results of [Mantz et al.(2014)] are overplotted as black crosses.
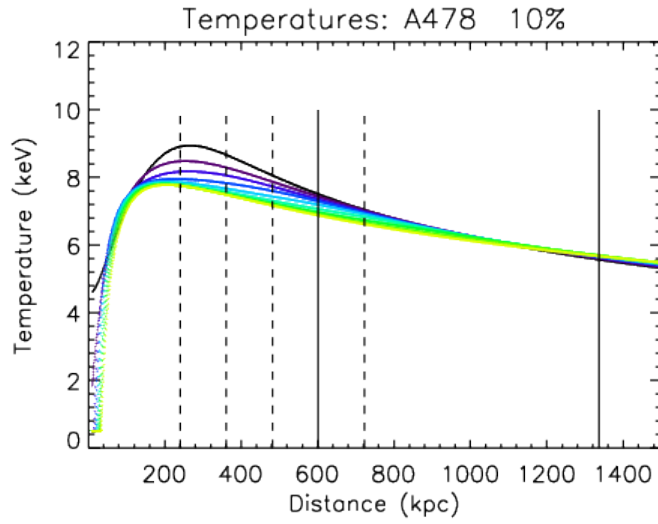
Figure 6.6: Same as figure 6.1, except for 10% conduction.
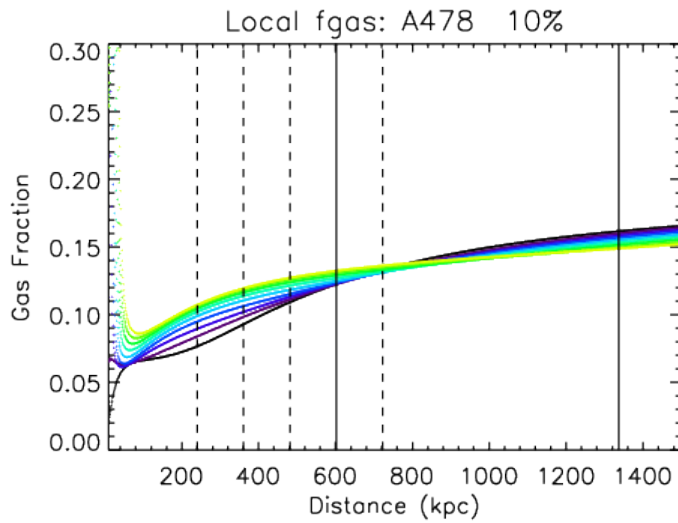
Figure 6.7: Same as figure 6.2, except for 10% conduction.
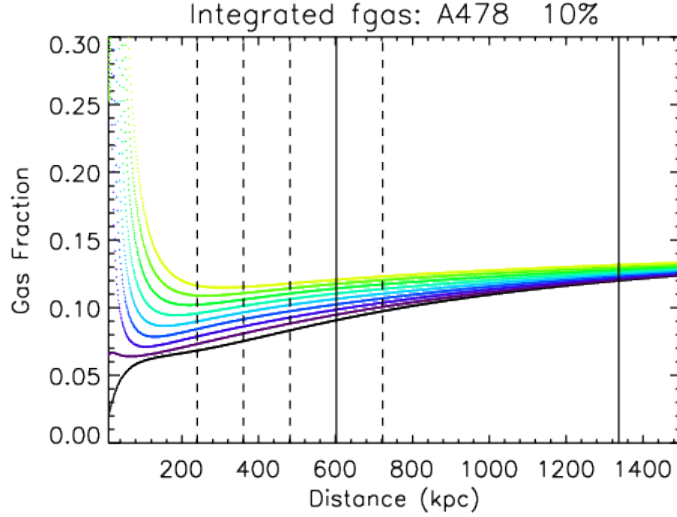
Figure 6.8: Same as figure 6.3, except for 10% conduction.

balance is maintained with the next bin). As the gas becomes more dense, cooling is more pronounced. This explains why conduction isn't sufficient to warm the gas after it begins this catastrophic cooling process. Note that we don't include any heating mechanisms which might affect these results. To account for this, we have run a version for each cluster with cooling turned off, which effectively simulates the extreme case of heating that is sufficient to counterbalance the radiative cooling.

6.1.2 Gas Density profiles

We also plot the local gas fraction, defined as the gas density divided by the total mass density. The first, most obvious feature of these graphs is that the density increases significantly at the center. This is due to the feedback mechanism described in Section 6.1.1. Also note that in the region of interest (between 0.4 and 1.2 of r_{2500}), there is significant difference in the gas fraction profiles between
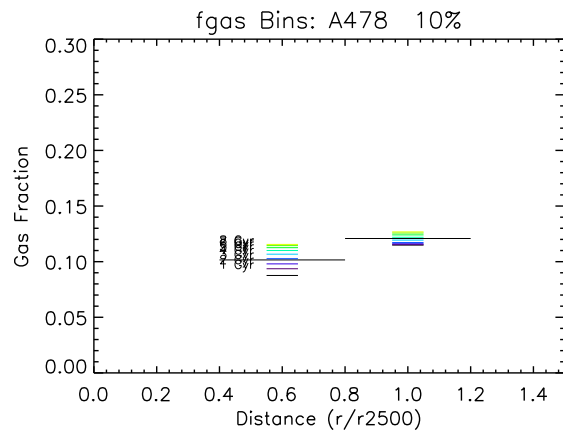
Figure 6.9: Same as figure 6.4, except for 10% conduction.
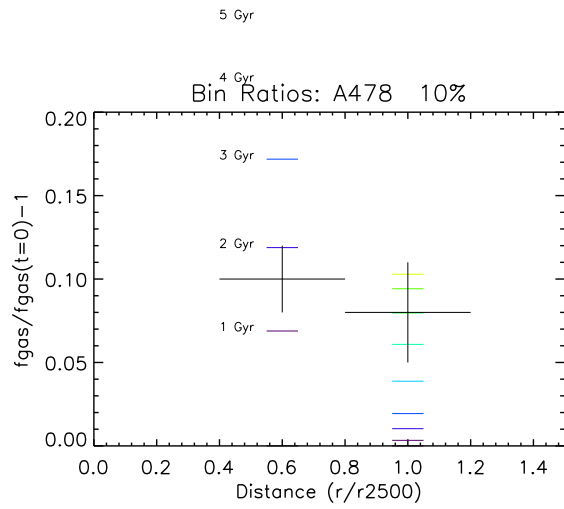
Figure 6.10: Same as figure 6.5, except for 10% conduction.
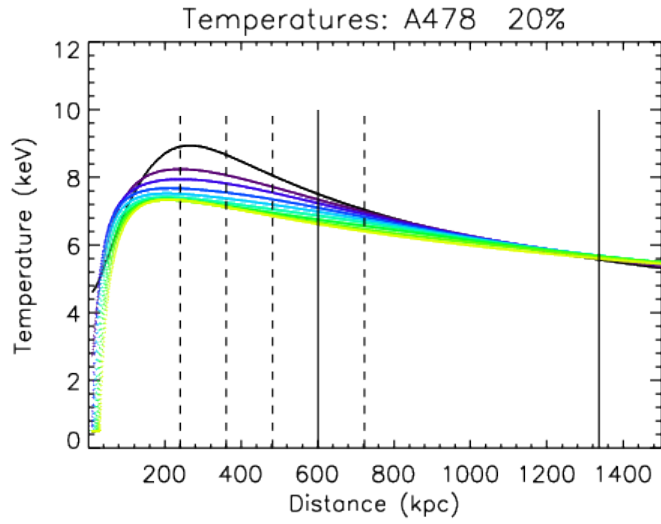
Figure 6.11: Same as figure 6.1, except for 20% conduction.
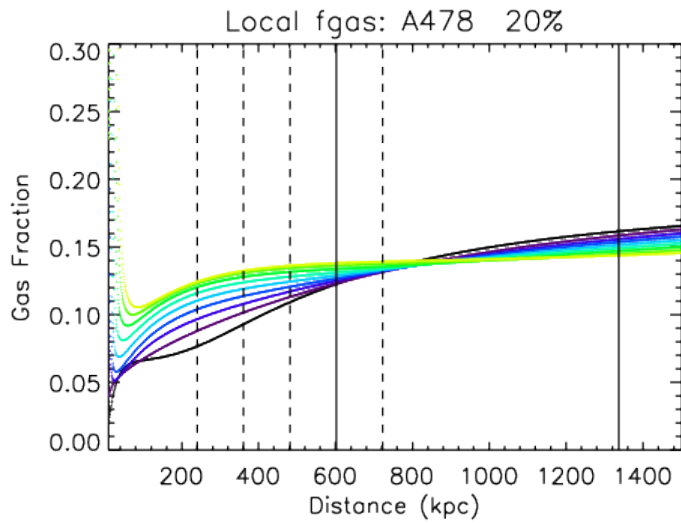
Figure 6.12: Same as figure 6.2, except for 20% conduction.
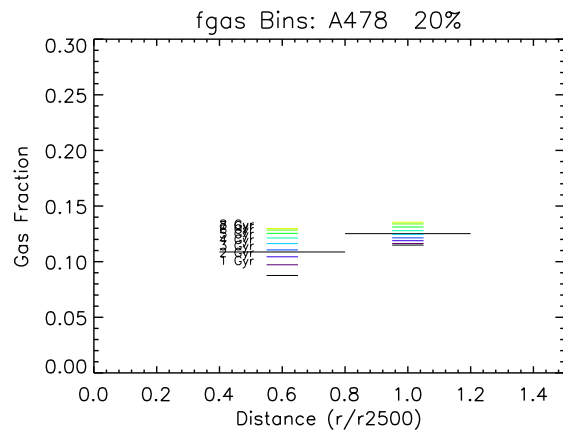
Figure 6.13: Same as figure 6.4, except for 20% conduction.
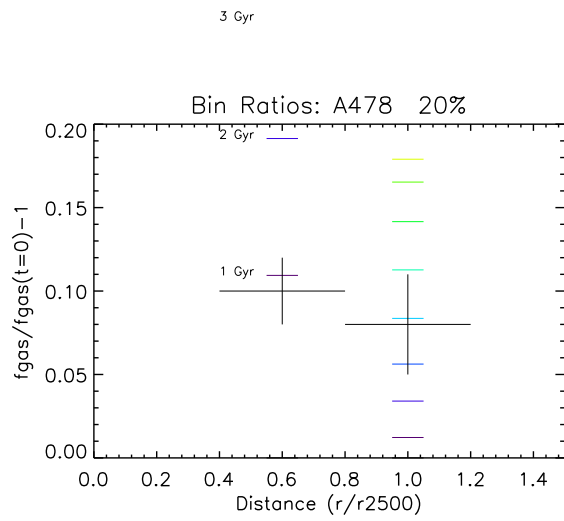
Figure 6.14: Same as figure 6.5, except for 20% conduction.

the different conduction factors. The spread over time increases with increasing conduction factor. This is also visible in the integrated gas fraction plots, where the integrated gas fraction is defined as the total gas mass within radius r divided by the total cluster mass within that same radius, as given by the NFW profile (Eq 4.2).

6.1.3 Binned Gas Fraction

Next we compare the binned gas fraction. For these plots, as described in Chapter 7, we have determined the total gas mass contained within bins of width $0.4r_{2500}$, centered at 0.6 and 1.0 of r_{2500}. Here also the difference between the different conduction factors is noticeable.

We also plot the fractional change in the gas fraction within these bins. We use this fractional change to compare to the results of [Mantz et al.(2014)], who have determined intrinsic scatter in gas fraction from a median value from among a sample of 40 clusters. The results of [Mantz et al.(2014)] are overplotted in the plots showing fractional change in gas fraction. We limit our comparisons to the first 5 Gyr. Note that for conduction suppression factors larger than 10%, the gas fraction increase in the bin from 0.4 - 0.8 r_{2500} already exceeds the scatter in [Mantz et al.(2014)], and only at 2% conduction is it the case that the fractional change in gas fraction at 5 Gyr is within the limits determined by [Mantz et al.(2014)].

6.1.4 Cooling test

We compare the results of the simulation with and without cooling for this cluster at 5% of Spitzer conduction, to determine whether cooling has a significant impact on our conclusions. Because radiative cooling is likely to be more complex in the core than we assume in our model without AGN feedback, we compare the results of an extreme case with no cooling, which corresponds to a case with heating that is sufficient to counter the cooling. In the radial range of interest (outside of the cool core), we find that there is no qualitative difference in the results with or without cooling. The result without cooling is presented in Figure 6.15.

6.2 A2029

Cluster A2029 has a cool core and has a semi-broad peak in the temperature profile at approximately 9 keV and average temperature outside of the cluster core of 8.5 keV. The grid of plots are shown in Figures 6.16 to 6.28.

The temperature profile plots of A2029 follow a similar pattern to the other clusters. With sufficient conduction, the core is able to warm to near the peak temperature before cooling, while with low conduction this doesn't happen. The gas fraction profiles show again significant differences in how much redistribution occurs. The binned gas fraction profiles show agreement with the results of [Mantz et al.(2014)] only at 2% of full Spitzer conduction, and are nearly in agreement for 3% and 5%.
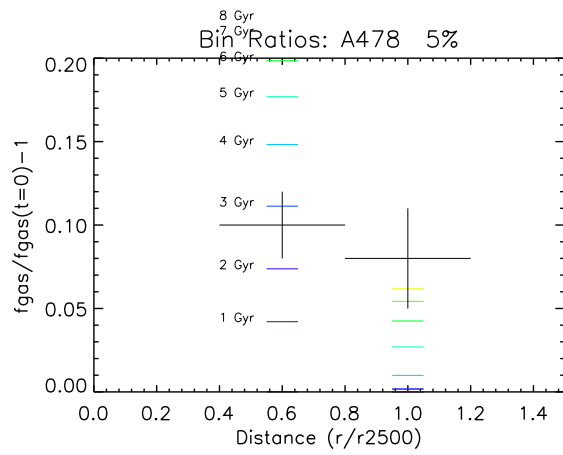
Figure 6.15: Same as figure 6.5, except for 5% conduction and with no cooling.
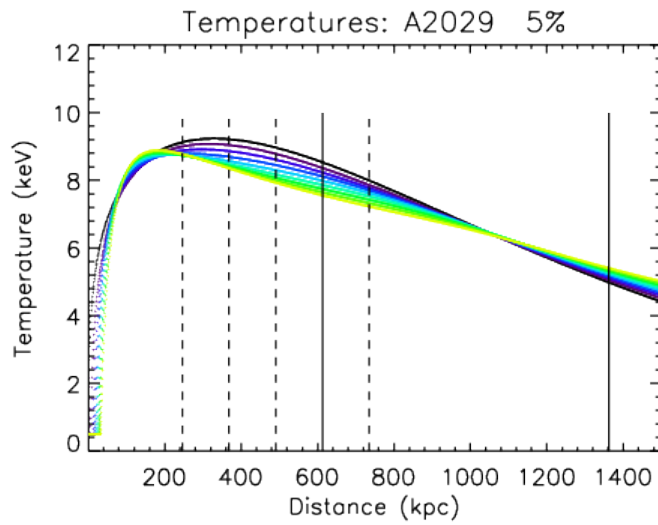
Figure 6.16: Temperature profiles, in 1 Gyr increments, for A2029 with a thermal conduction factor of 5%. The black curve represents the initial profile. Solid vertical lines are plotted at r_{2500} and r_{500}, and dashed lines are plotted at 0.4, 0.6, 0.8, and 1.2 of r_{2500}.
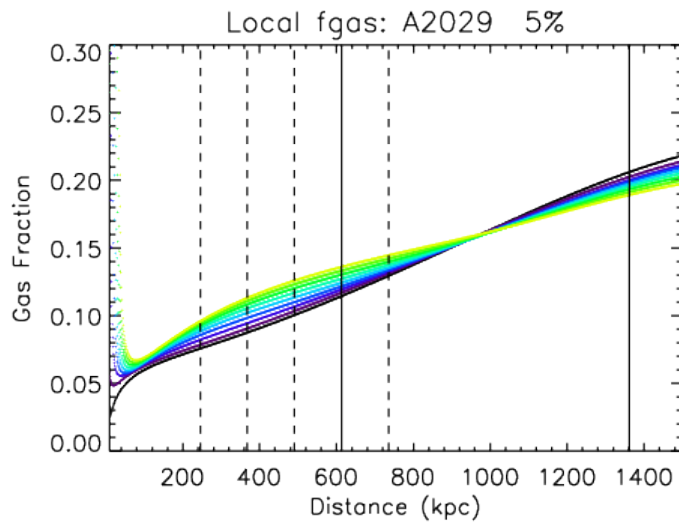
Figure 6.17: Gas fraction profiles, in 1 Gyr increments, for A2029 with a thermal conduction factor of 5%. The black curve represents the initial profile. Solid vertical lines are plotted at r_{2500} and r_{500}, and dashed lines are plotted at 0.4, 0.6, 0.8, and 1.2 of r_{2500}.
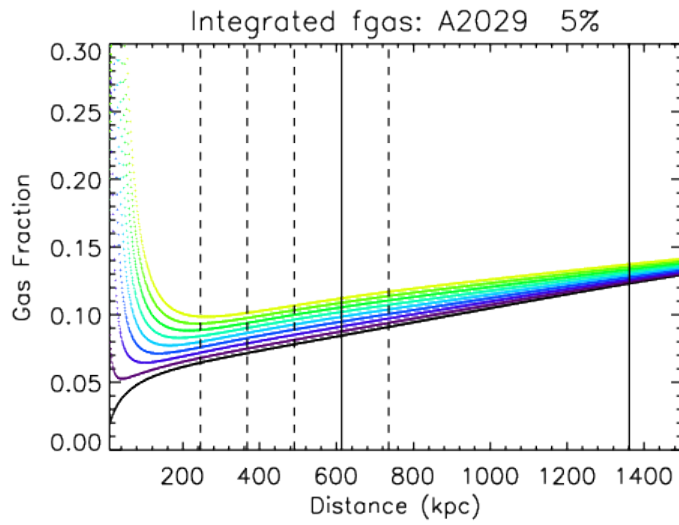
Figure 6.18: Integrated gas fraction profiles, in 1 Gyr increments, for A2029 with a thermal conduction factor of 5%. The black curve represents the initial profile. Solid vertical lines are plotted at r_{2500} and r_{500}, and dashed lines are plotted at 0.4, 0.6, 0.8, and 1.2 of r_{2500}.
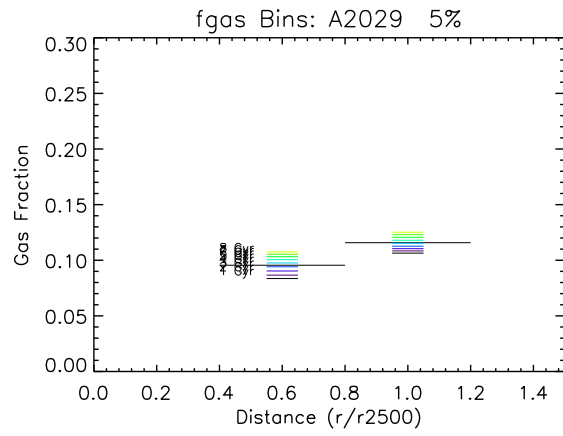
Figure 6.19: Binned gas fraction, in 1 Gyr increments, for A2029 with a thermal conduction factor of 5%, plotted as a function of r/r_{2500}.
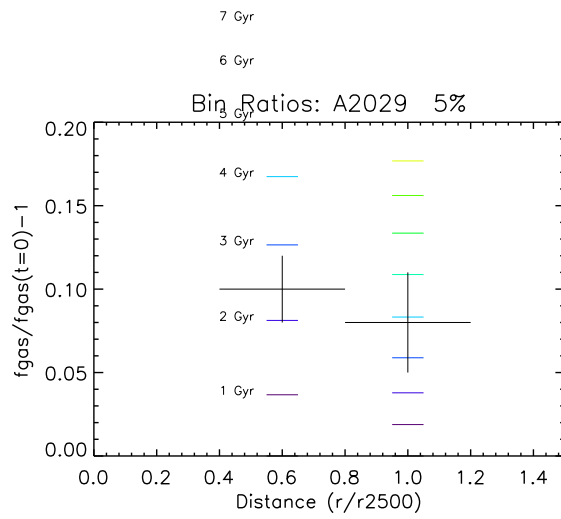
Figure 6.20: Fractional change in binned gas fraction, in 1 Gyr increments, for A2029 with a thermal conduction factor of 5%, plotted as a function of r/r_{2500}. The intrinsic scatter results of [Mantz et al.(2014)] are overplotted as black crosses.
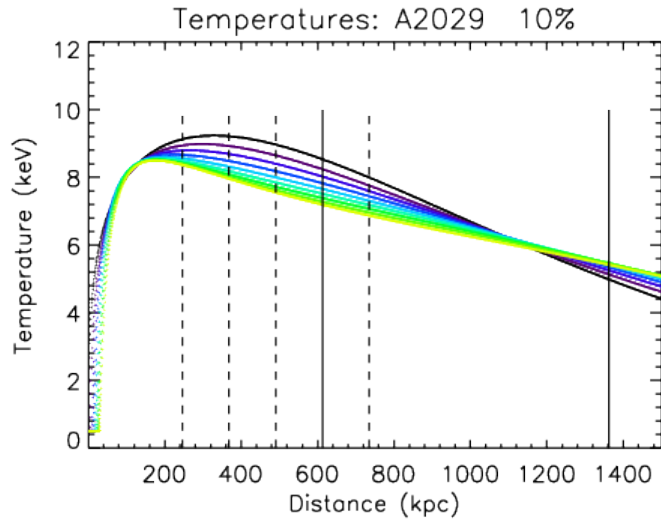
Figure 6.21: Same as figure 6.16, except for 10% conduction.
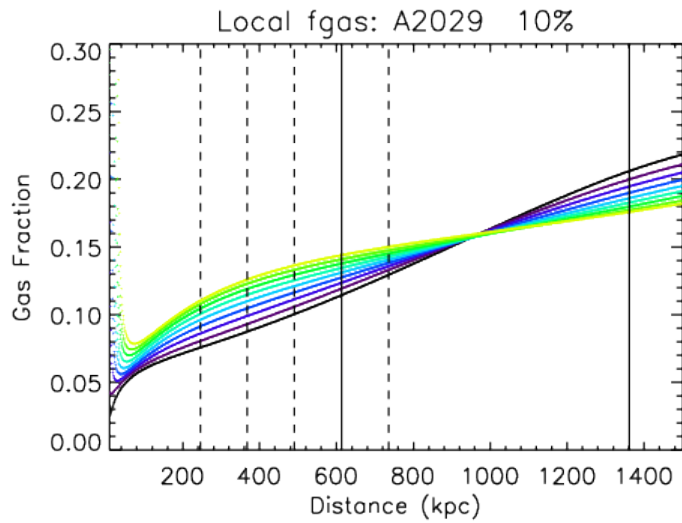
Figure 6.22: Same as figure 6.17, except for 10% conduction.
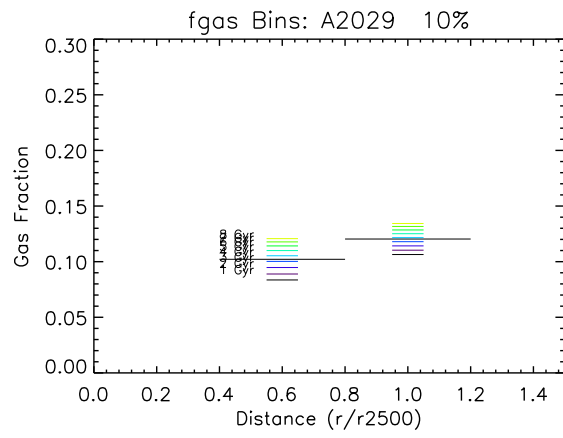
Figure 6.23: Same as figure 6.19, except for 10% conduction.
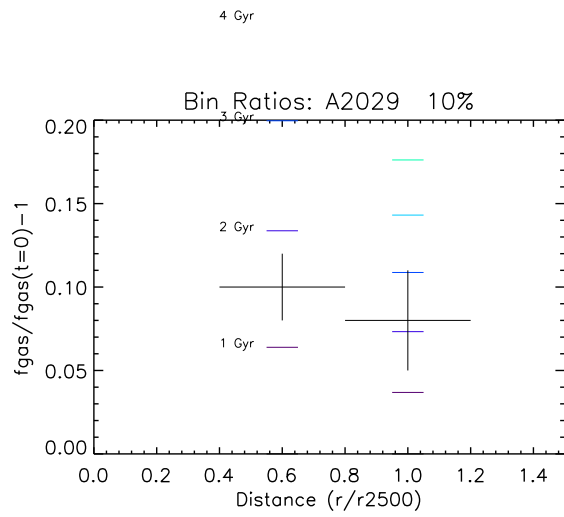
Figure 6.24: Same as figure 6.20, except for 10% conduction.
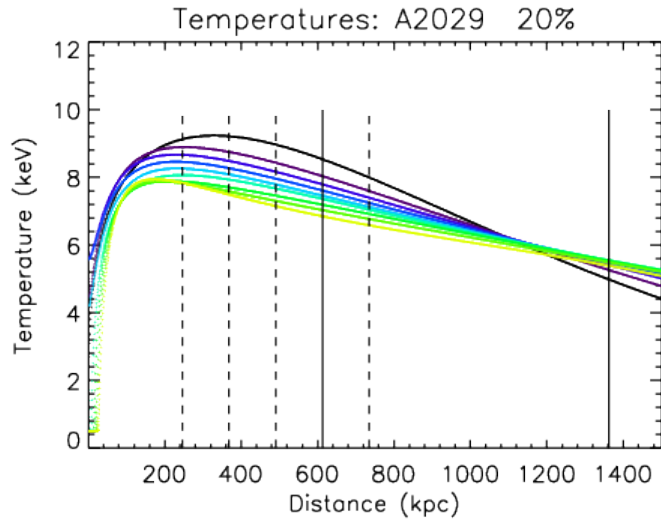
Figure 6.25: Same as figure 6.16, except for 20% conduction.
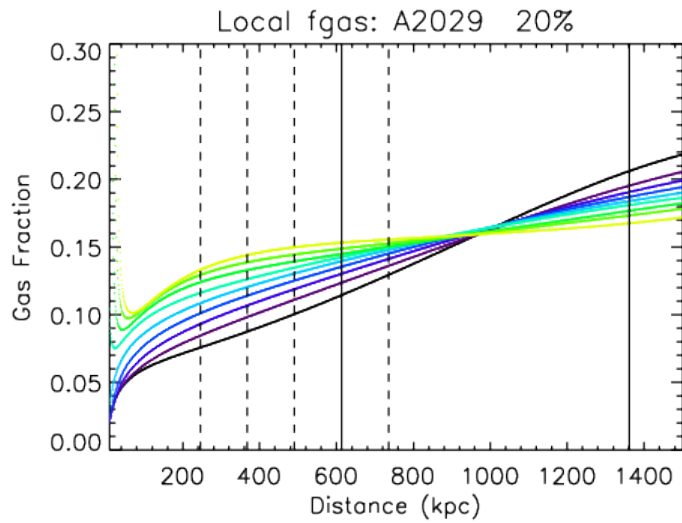
Figure 6.26: Same as figure 6.17, except for 20% conduction.
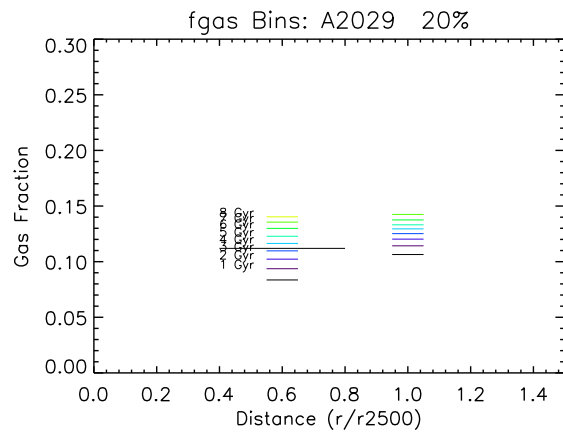
Figure 6.27: Same as figure 6.19, except for 20% conduction.
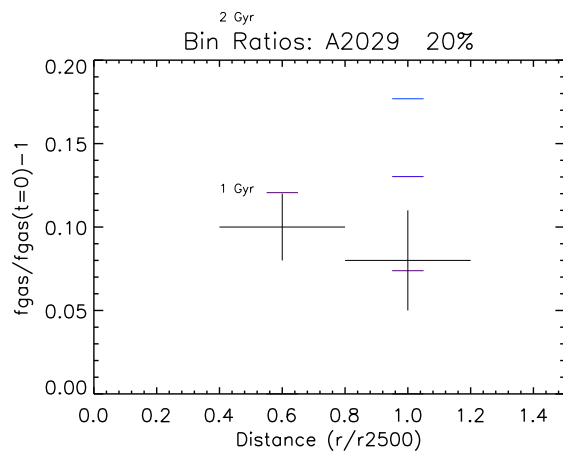
Figure 6.28: Same as figure 6.20, except for 20% conduction.
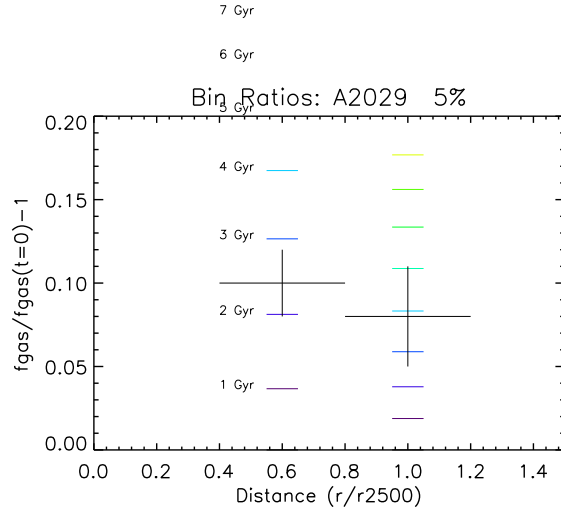
Figure 6.29: Same as figure 6.20, except for 5% conduction and with no cooling.

6.2.1 Cooling test

We compare the results of the simulation with and without cooling for this cluster at 5% of Spitzer conduction, to determine whether cooling has a significant impact on our conclusions. We find here also that there is no qualitative difference in the region of interest. The result without cooling is presented in Figure 6.29.
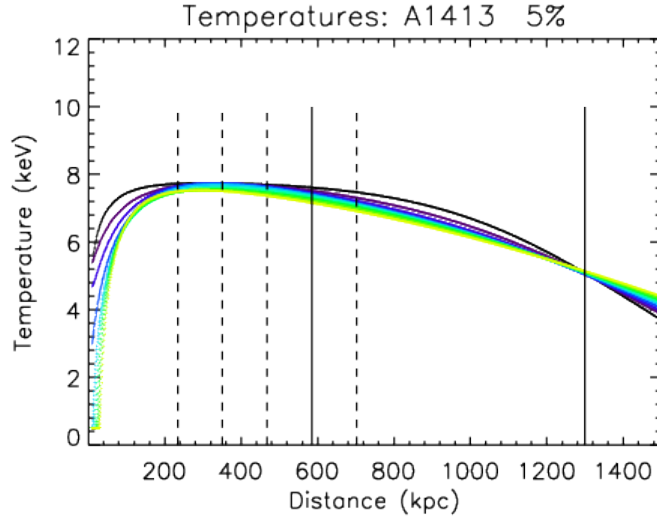
Figure 6.30: Temperature profiles, in 1 Gyr increments, for A1413 with a thermal conduction factor of 5%. The black curve represents the initial profile. Solid vertical lines are plotted at r_{2500} and r_{500}, and dashed lines are plotted at 0.4, 0.6, 0.8, and 1.2 of r_{2500}.

6.3   A1413

Cluster A1413 has a cool core and has a broad peak in the temperature profile at approximately 7.5 keV and average temperature outside of the cluster core of 7.3 keV. The grid of plots are shown in Figures 6.30 to 6.42.

Once again, we have similar qualitative behavior in the temperature profiles. With a large conduction factor, the cool core is able to heat to approximately the temperature of the wide peak before entering a cooling phase, while low values of conduction do not allow this heating. The gas density profiles show that with high values of conduction, there is significantly more change in the gas fraction when compared to the lower conduction values. Again we note the density peak at the

75
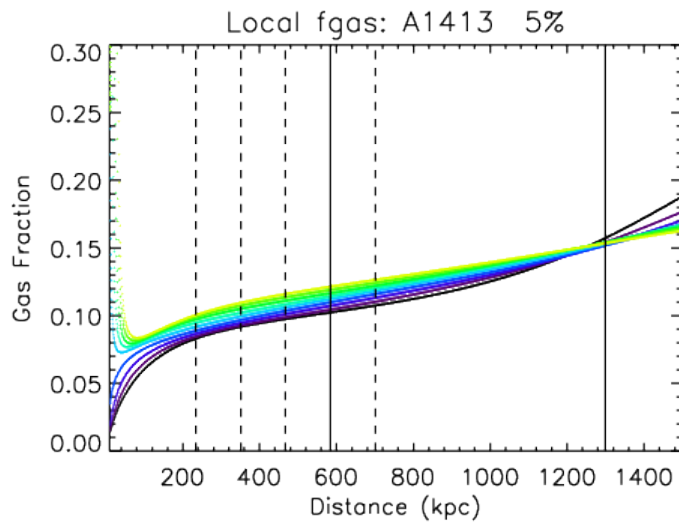
Figure 6.31: Gas fraction profiles, in 1 Gyr increments, for A1413 with a thermal conduction factor of 5%. The black curve represents the initial profile. Solid vertical lines are plotted at r_{2500} and r_{500}, and dashed lines are plotted at 0.4, 0.6, 0.8, and 1.2 of r_{2500}.
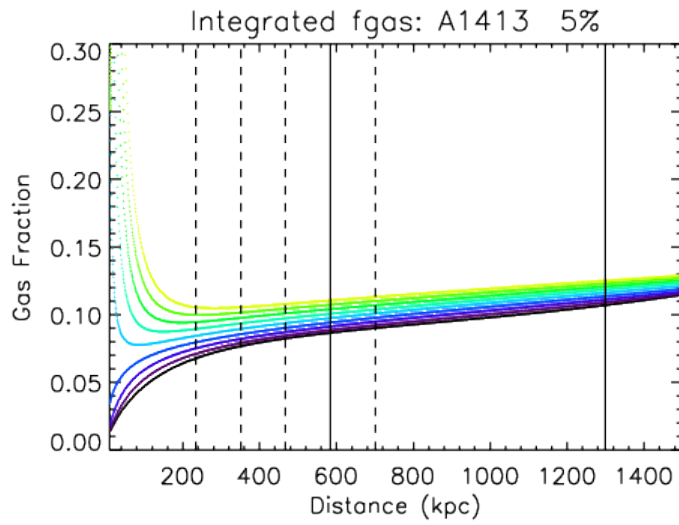
Figure 6.32: Integrated gas fraction profiles, in 1 Gyr increments, for A1413 with a thermal conduction factor of 5%. The black curve represents the initial profile. Solid vertical lines are plotted at r_{2500} and r_{500}, and dashed lines are plotted at 0.4, 0.6, 0.8, and 1.2 of r_{2500}.

Figure 6.33: Binned gas fraction, in 1 Gyr increments, for A1413 with a thermal conduction factor of 5%, plotted as a function of r/r_{2500}.
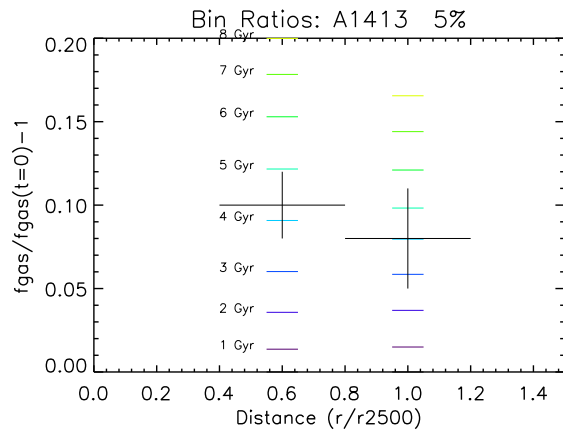
Figure 6.34: Fractional change in binned gas fraction, in 1 Gyr increments, for A1413 with a thermal conduction factor of 5%, plotted as a function of r/r_{2500}. The intrinsic scatter results of [Mantz et al.(2014)] are overplotted as black crosses.
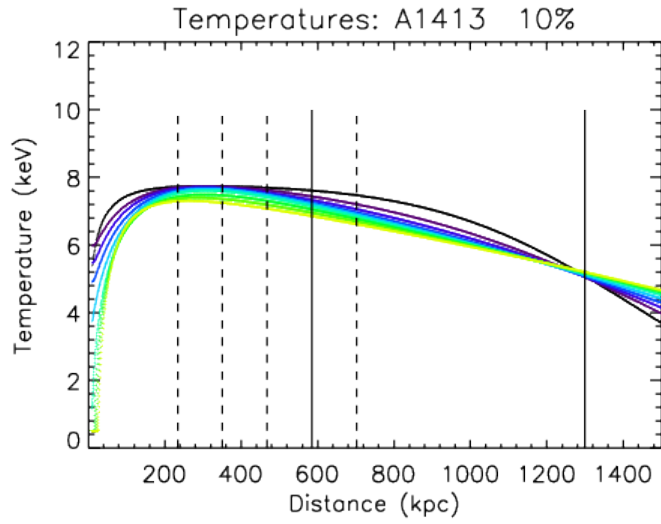
Figure 6.35: Same as figure 6.30, except for 10% conduction.
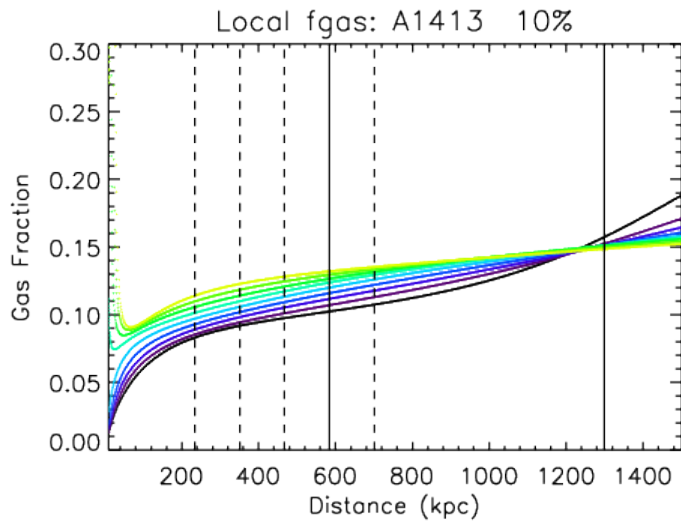
Figure 6.36: Same as figure 6.31, except for 10% conduction.
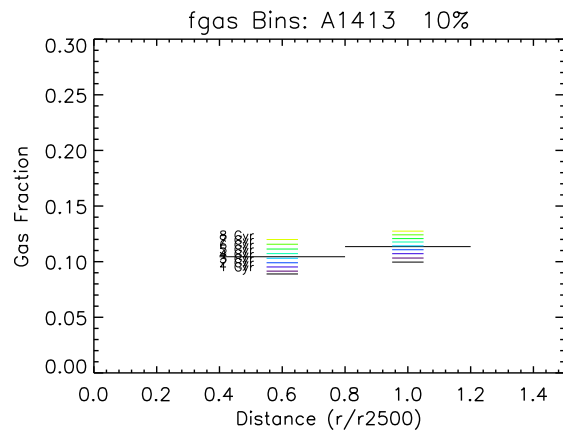
Figure 6.37: Same as figure 6.33, except for 10% conduction.
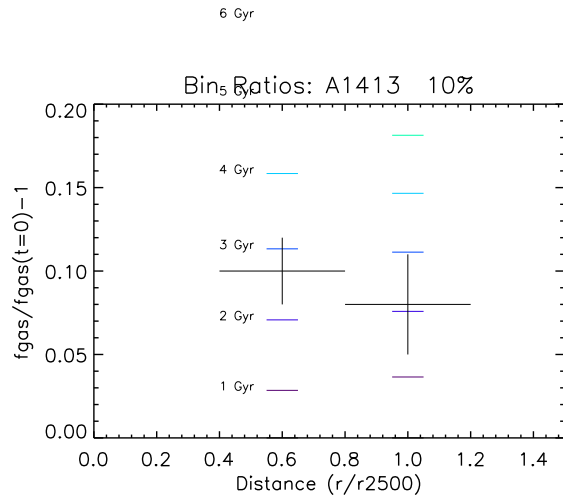
Figure 6.38: Same as figure 6.34, except for 10% conduction.
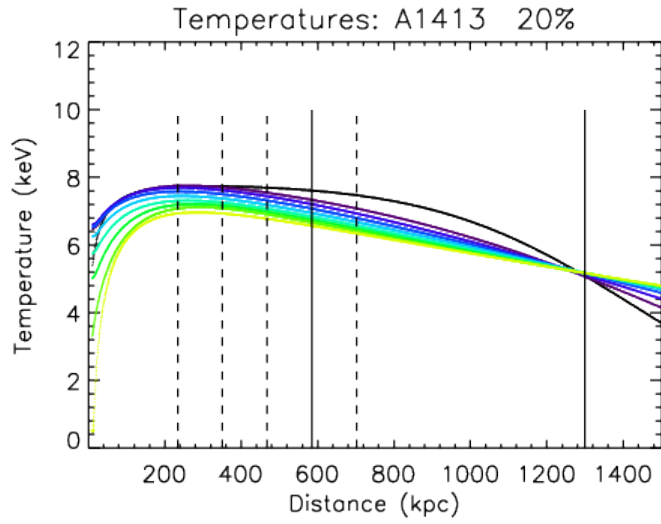
Figure 6.39: Same as figure 6.30, except for 20% conduction.
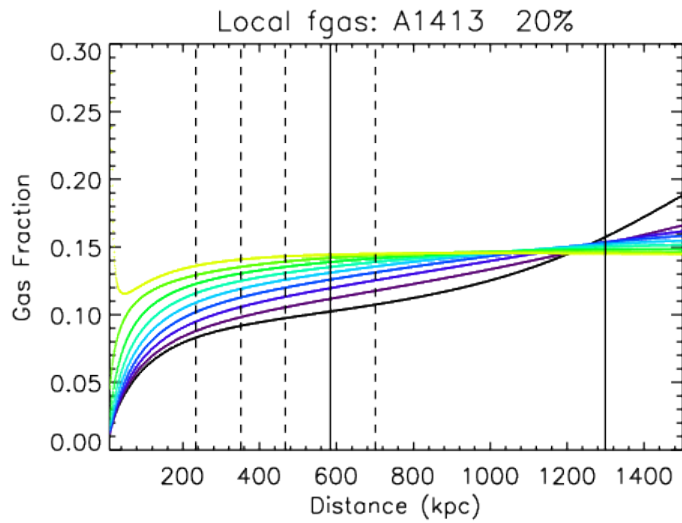
Figure 6.40: Same as figure 6.31, except for 20% conduction.
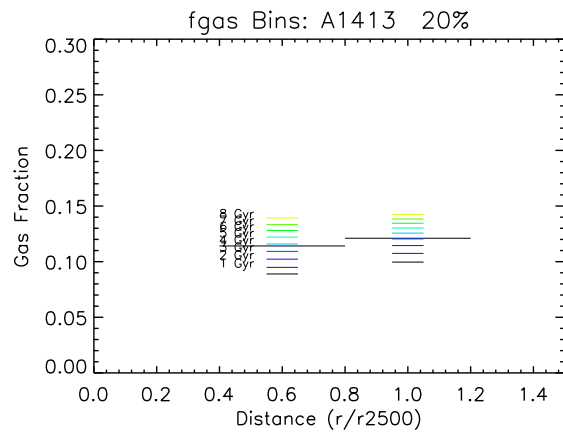
Figure 6.41: Same as figure 6.33, except for 20% conduction.
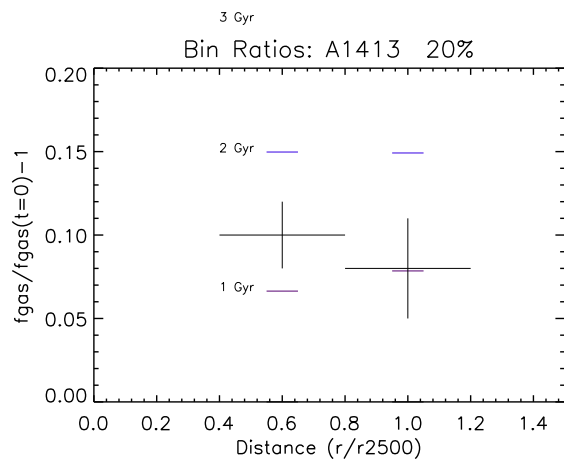
Figure 6.42: Same as figure 6.34, except for 20% conduction.

center due to the cooling feedback.

From the binned gas fraction plots, we note that with this cluster, a 5% conduction factor is consistent with the results of [Mantz et al.(2014)], given that the percent change in gas fraction in the 0.4 - 0.8 r_{2500} bin at 5 Gyr agrees with their observed scatter in gas fraction. However, the results for 10% conduction are not in agreement.

6.3.1   Cooling test

We compare the results of the simulation with and without cooling for this cluster at 5% of Spitzer conduction, to determine whether cooling has a significant impact on our conclusions. As before, there is no qualitative difference between the results with and without cooling turned on, in the region of interest. The result without cooling is presented in Figure 6.43.

6.4   A907

Cluster A907, as shown in Chapter 7, has a peak temperature of approximately 7 keV and average temperature outside of the cluster core of 5.9 keV. The grid of plots are shown in Figures 6.44 to 6.57.

The temperature at the core of A907 behaves in a way similar to A478. If the conduction factor is low enough, there isn't sufficient thermal conduction to heat the core, and cooling dominates. Even with high conduction values, the core still eventually cools, due to the same effect as seen in A478.
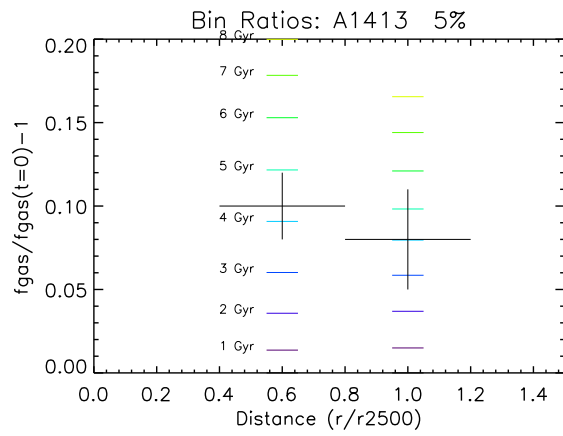
Figure 6.43: Same as figure 6.34, except for 5% conduction and with no cooling.
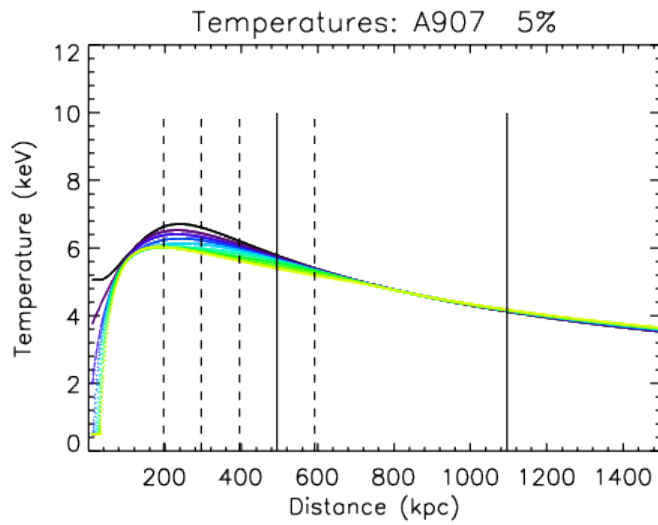
Figure 6.44: Temperature profiles, in 1 Gyr increments, for A907 with a thermal conduction factor of 5%. The black curve represents the initial profile. Solid vertical lines are plotted at r_{2500} and r_{500}, and dashed lines are plotted at 0.4, 0.6, 0.8, and 1.2 of r_{2500}.
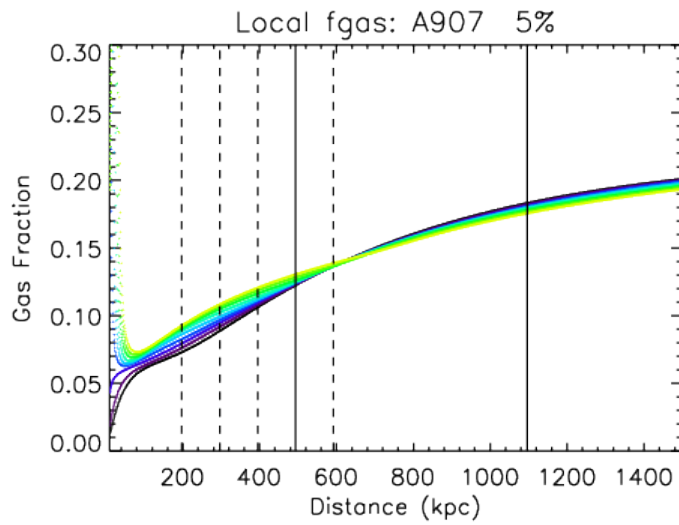
Figure 6.45: Gas fraction profiles, in 1 Gyr increments, for A907 with a thermal conduction factor of 5%. The black curve represents the initial profile. Solid vertical lines are plotted at r_{2500} and r_{500}, and dashed lines are plotted at 0.4, 0.6, 0.8, and 1.2 of r_{2500}.
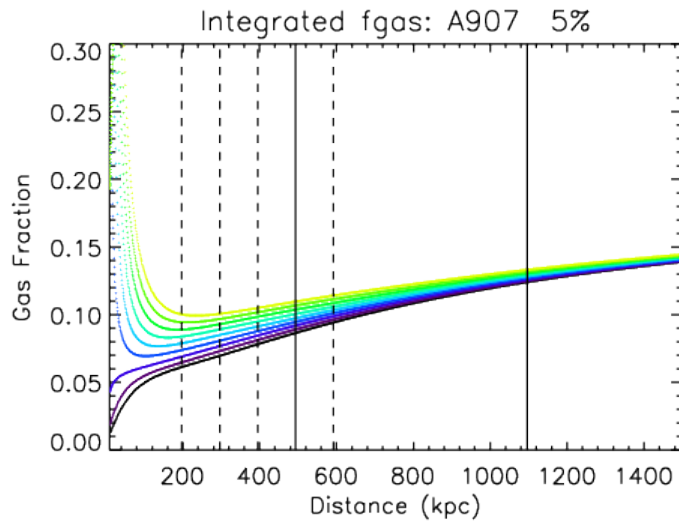
Figure 6.46: Integrated gas fraction profiles, in 1 Gyr increments, for A907 with a thermal conduction factor of 5%. The black curve represents the initial profile. Solid vertical lines are plotted at r_{2500} and r_{500}, and dashed lines are plotted at 0.4, 0.6, 0.8, and 1.2 of r_{2500}.
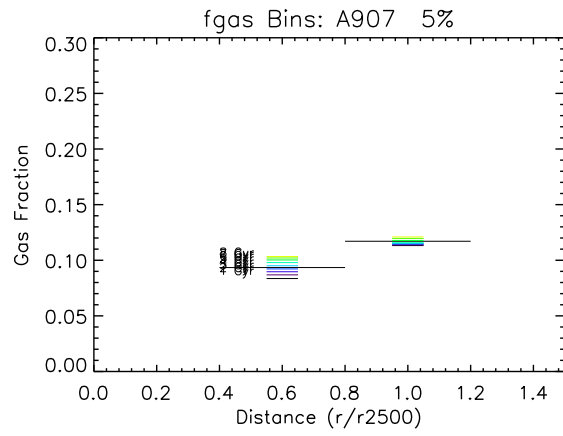
Figure 6.47: Binned gas fraction, in 1 Gyr increments, for A907 with a thermal conduction factor of 5%, plotted as a function of r/r_{2500}.
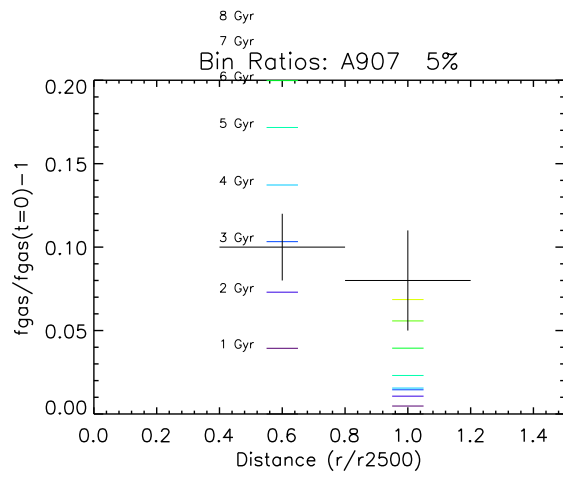
Figure 6.48: Fractional change in binned gas fraction, in 1 Gyr increments, for A907 with a thermal conduction factor of 5%, plotted as a function of r/r_{2500}. The intrinsic scatter results of [Mantz et al.(2014)] are overplotted as black crosses.
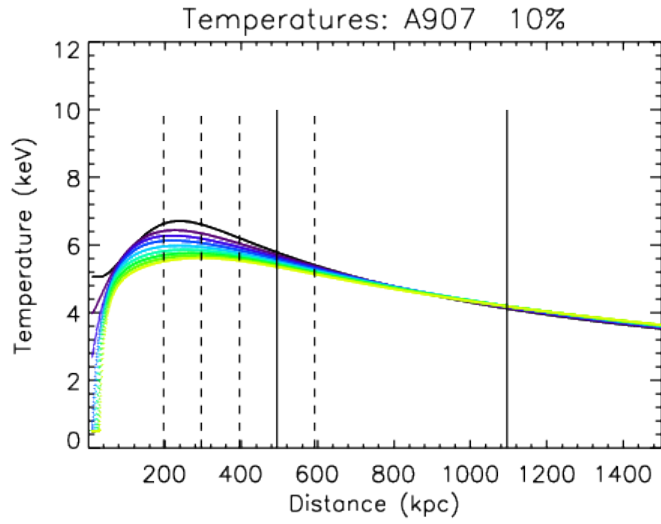
Figure 6.49: Same as figure 6.44, except for 10% conduction.
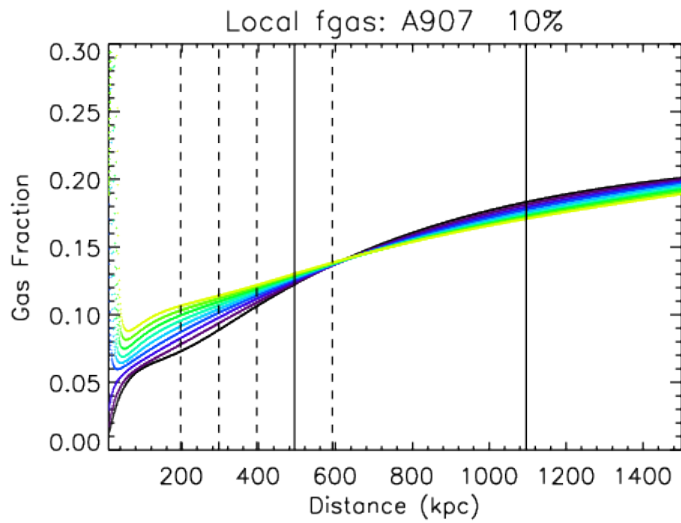
Figure 6.50: Same as figure 6.45, except for 10% conduction.
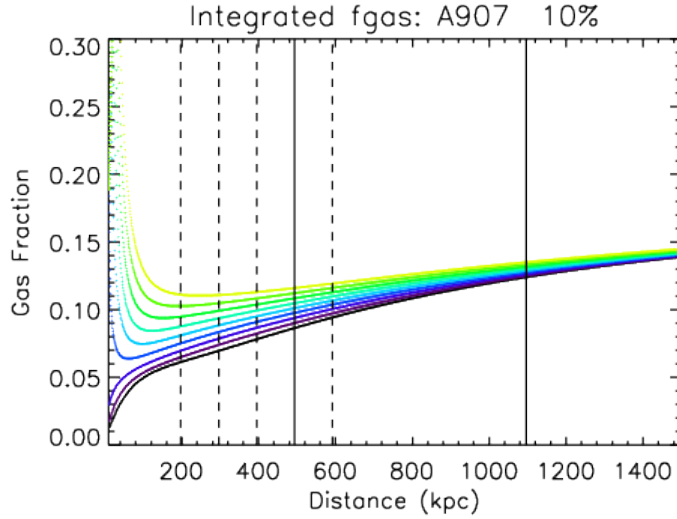
Figure 6.51: Same as figure 6.46, except for 10% conduction.

We also plot the local gas fraction and integrated gas fraction for A907. Here again, we see the large spike in density at the core due to the cooling there, and again we see that the change in density in the region of interest is significantly smaller for low conduction compared to high conduction.

Next we compare the binned gas fraction and the fractional change in these bins. We note that the bin at 5 Gyr is within the limits of Mantz only at 2% conduction again.

6.4.1 Cooling test

We compare the results of the simulation with and without cooling for this cluster at 5% of Spitzer conduction, to determine whether cooling has a significant impact on our conclusions. We again find no qualitative difference in the region of interest. The result without cooling is presented in Figure 6.58.
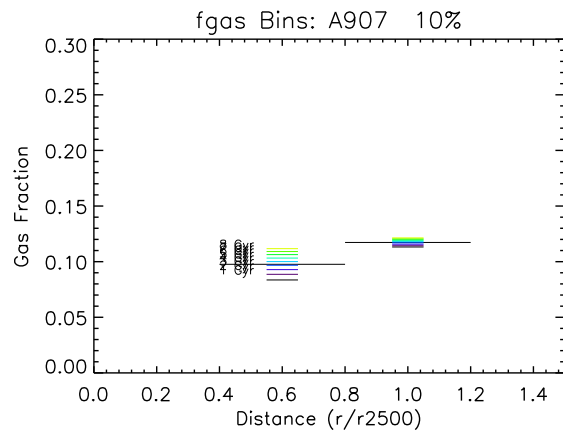
Figure 6.52: Same as figure 6.47, except for 10% conduction.
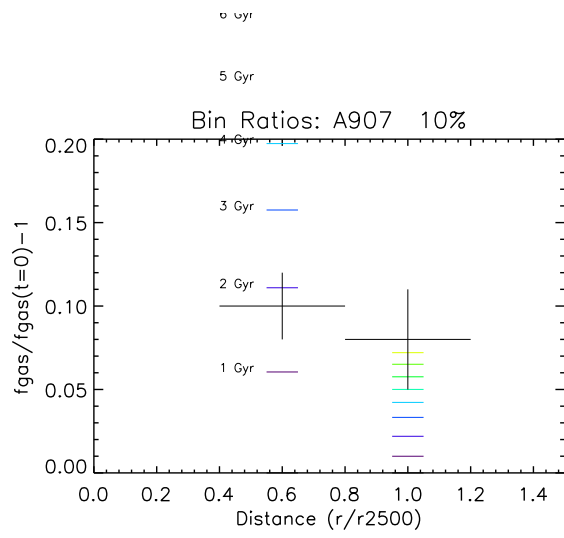
Figure 6.53: Same as figure 6.48, except for 10% conduction.
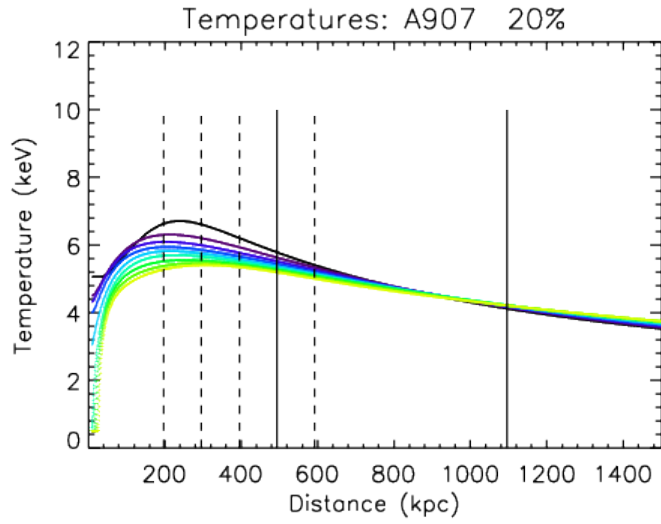
Figure 6.54: Same as figure 6.44, except for 20% conduction.
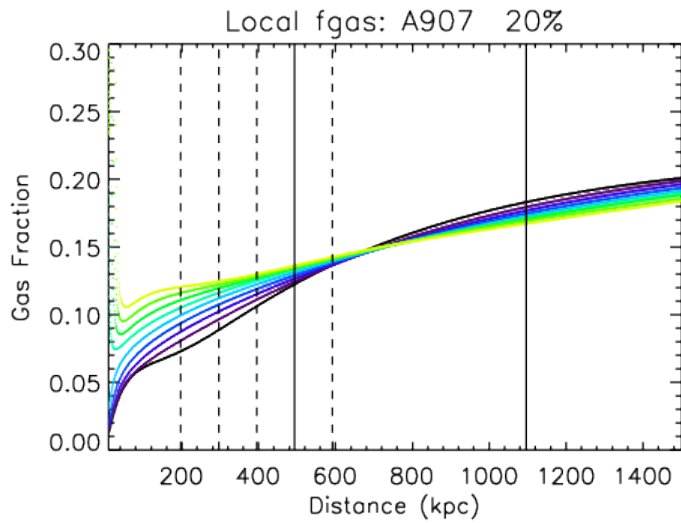
Figure 6.55: Same as figure 6.45, except for 20% conduction.

Figure 6.56: Same as figure 6.47, except for 20% conduction.
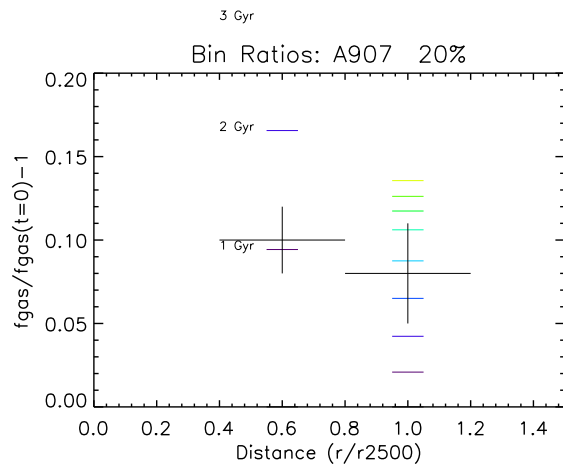
Figure 6.57: Same as figure 6.48, except for 20% conduction.
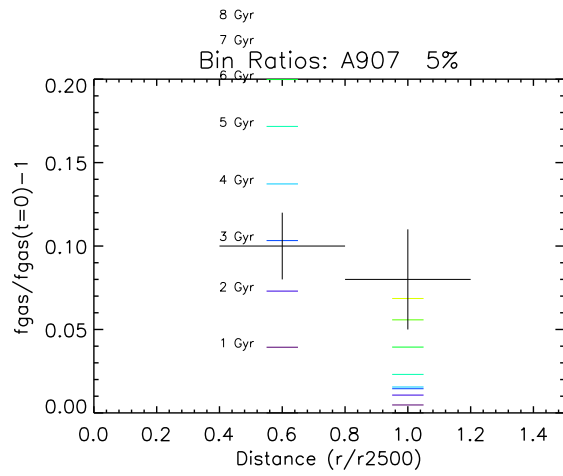
Figure 6.58: Same as figure 6.48, except for 5% conduction and with no cooling.
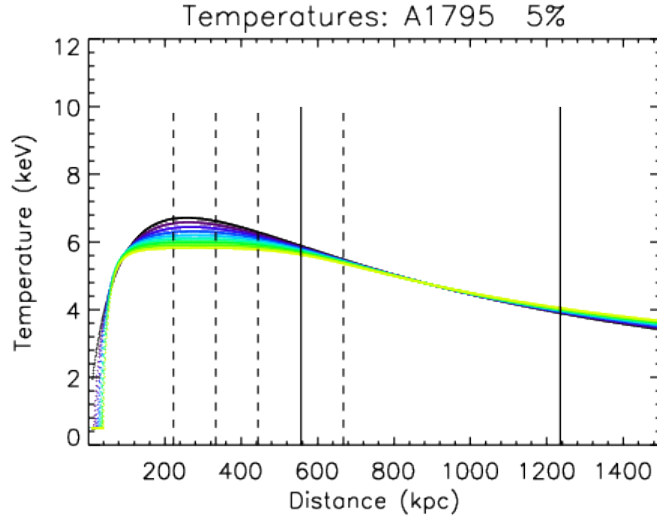
Figure 6.59: Temperature profiles, in 1 Gyr increments, for A1795 with a thermal conduction factor of 5%. The black curve represents the initial profile. Solid vertical lines are plotted at r_{2500} and r_{500}, and dashed lines are plotted at 0.4, 0.6, 0.8, and 1.2 of r_{2500}.

6.5 A1795

Cluster A1795 has a cool core and has a peak in the temperature profile at approximately 7 keV and average temperature outside of the cluster core of 6.1 keV. The grid of plots are shown in Figures 6.59 to 6.72.

Cluster A1795 has slightly different behavior at the core than do the other clusters in this study. Even at high conduction (50%), thermal conduction is not sufficient to raise the temperature of the core to near the peak temperature. There is some warming, but cooling is strong enough to keep the core at relatively low temperatures. It is noteworthy that the gas fraction at the core of this cluster is higher than in the other clusters of this study. Since cooling is proportional to the
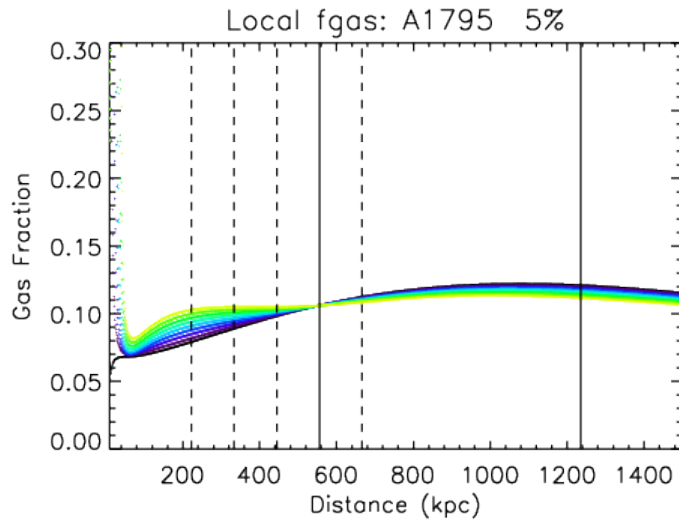
Figure 6.60: Gas fraction profiles, in 1 Gyr increments, for A1795 with a thermal conduction factor of 5%. The black curve represents the initial profile. Solid vertical lines are plotted at r_{2500} and r_{500}, and dashed lines are plotted at 0.4, 0.6, 0.8, and 1.2 of r_{2500}.
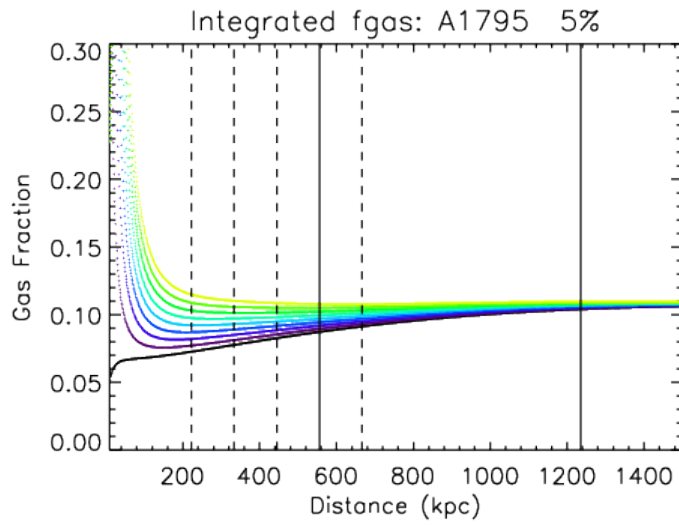
Figure 6.61: Integrated gas fraction profiles, in 1 Gyr increments, for A1795 with a thermal conduction factor of 5%. The black curve represents the initial profile. Solid vertical lines are plotted at r_{2500} and r_{500}, and dashed lines are plotted at 0.4, 0.6, 0.8, and 1.2 of r_{2500}.
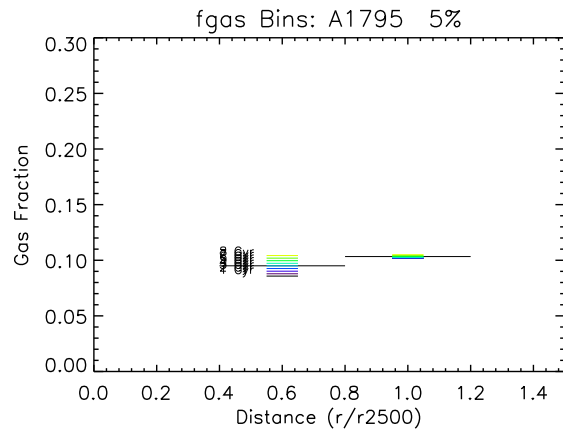
Figure 6.62: Binned gas fraction, in 1 Gyr increments, for A1795 with a thermal conduction factor of 5%, plotted as a function of r/r_{2500}.
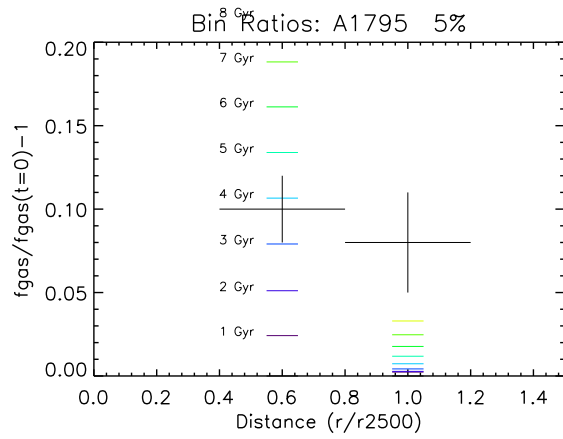
Figure 6.63: Fractional change in binned gas fraction, in 1 Gyr increments, for A1795 with a thermal conduction factor of 5%, plotted as a function of r/r_{2500}. The intrinsic scatter results of [Mantz et al.(2014)] are overplotted as black crosses.
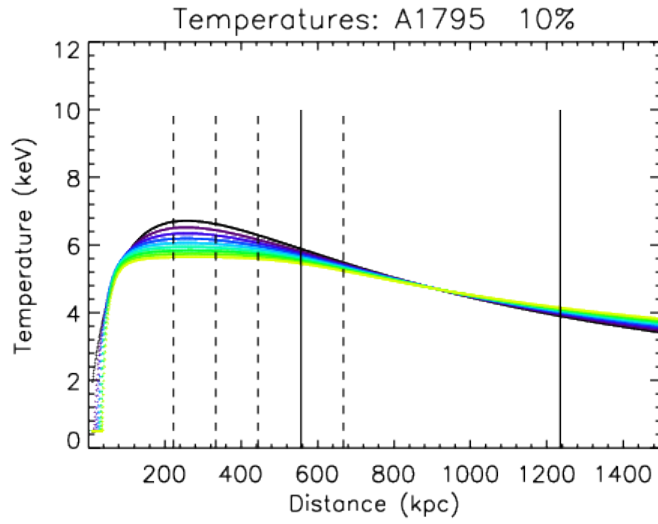
Figure 6.64: Same as figure 6.59, except for 10% conduction.
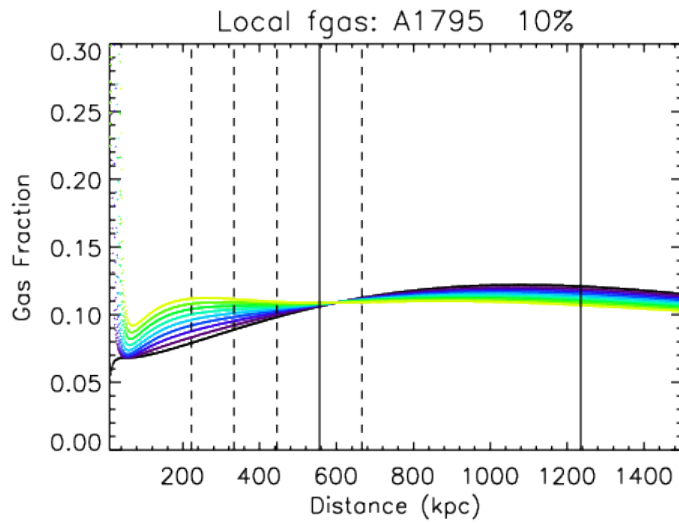
Figure 6.65: Same as figure 6.60, except for 10% conduction.
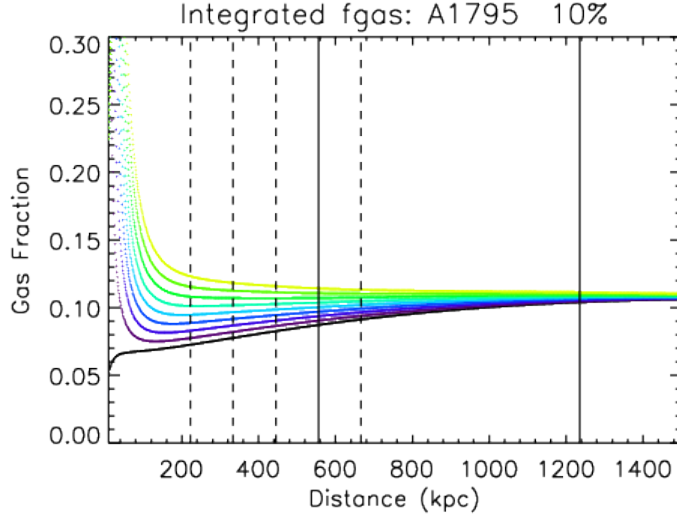
Figure 6.66: Same as figure 6.61, except for 10% conduction.

square of the gas density, this may be part of the reason for this difference.

There is again a significant difference in the gas fraction profiles, as in all of the clusters in this study. It is interesting to note that the point at which the gas fraction remains constant shifts outward from the cluster, from less than r_{2500} at 2 and 3% of full conduction to $1.2r_{2500}$ at 50% conduction.

In the binned fgas plots, we note that again conduction factors greater than 10% result in disagreement with the conclusions of [Mantz et al.(2014)]. 2 and 3% conduction give results that are in full agreement, and 5% is in agreement for the first 4 Gyr.

6.5.1 Cooling test

We compare the results of the simulation with and without cooling for this cluster at 5% of Spitzer conduction, to determine whether cooling has a significant
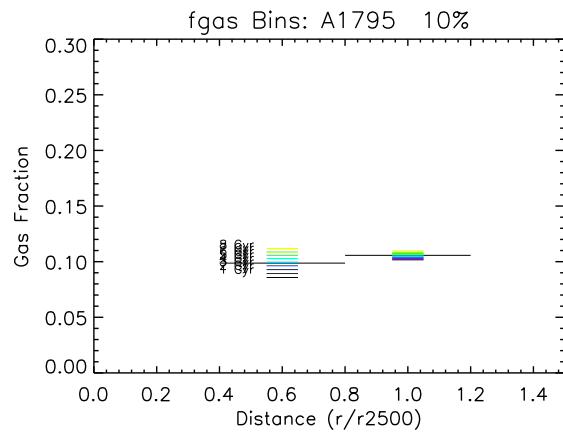
Figure 6.67: Same as figure 6.62, except for 10% conduction.
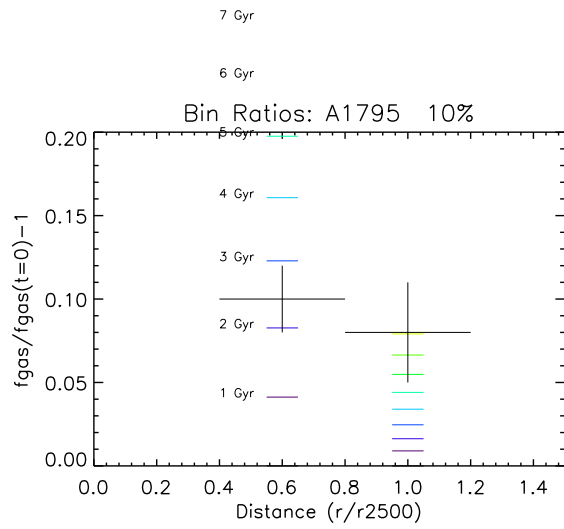
Figure 6.68: Same as figure 6.63, except for 10% conduction.
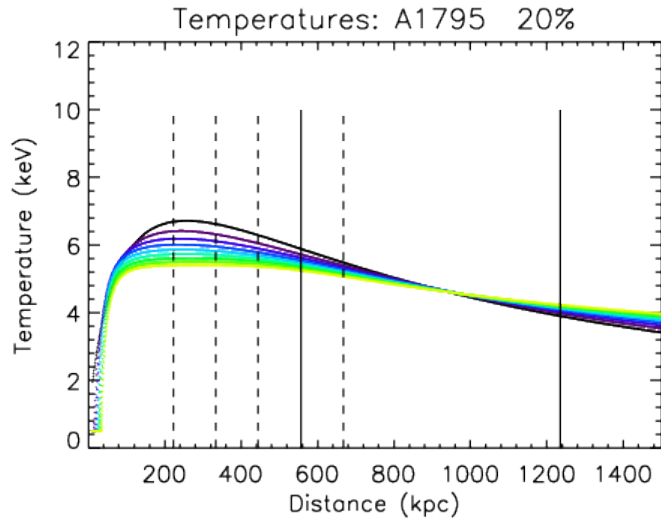
Figure 6.69: Same as figure 6.59, except for 20% conduction.
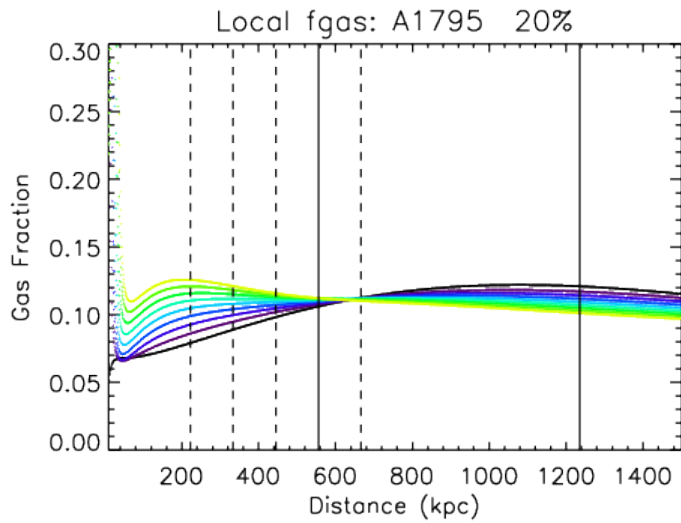
Figure 6.70: Same as figure 6.60, except for 20% conduction.
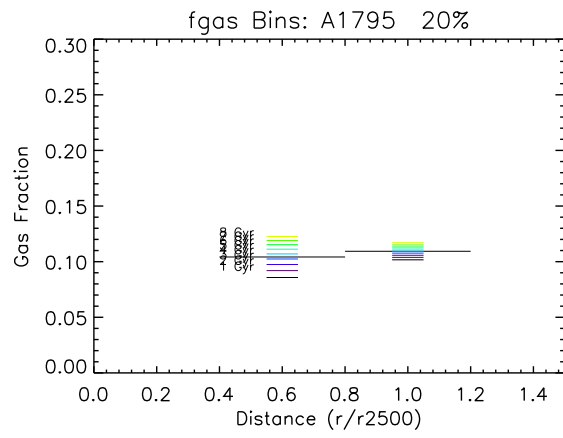
Figure 6.71: Same as figure 6.62, except for 20% conduction.
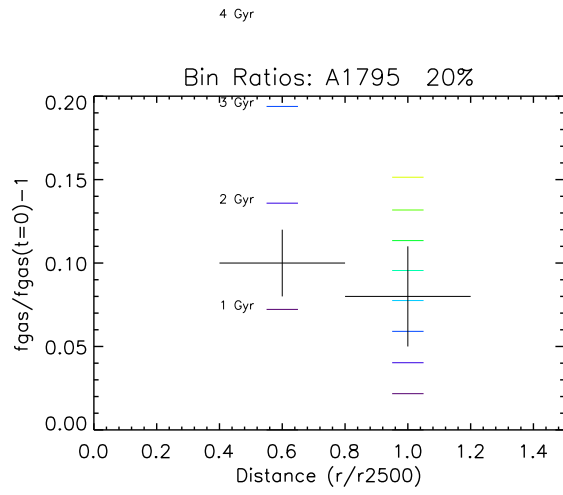
Figure 6.72: Same as figure 6.63, except for 20% conduction.
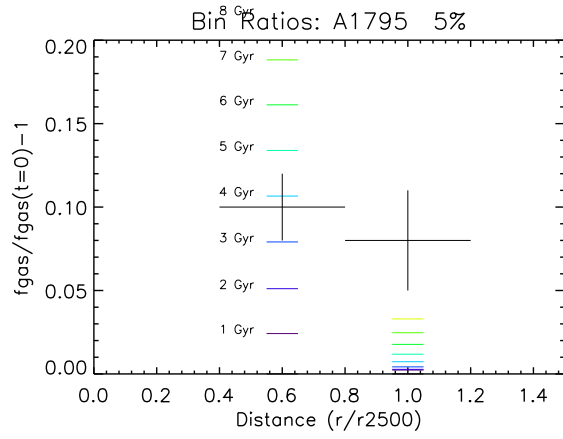
Figure 6.73: Same as figure 6.63, except for 5% conduction and with no cooling.

impact on our conclusions. Here again, no qualitative difference in the region of interest is noted. The result without cooling is presented in Figure 6.73.

6.6   Discussion of Results

We are comparing our results to those of [Mantz et al.(2014)], who have determined the scatter in the gas fraction of hot, relaxed clusters. In order to compare, we look at the fractional change in the gas fraction between the initial profile and

the profile several Gyr later, in increments of 1 Gyr. With the assumption that the sample used by [Mantz et al.(2014)] contains clusters with varying ages, we look at how the gas fraction changes with age.

For each cluster in our sample, we determine that one result of thermal conduction is a redistribution of the intracluster gas. This change in the gas fraction due simply from the aging of the cluster will result in a scatter in the observed gas fraction of any sample of clusters with varying ages. That is, as a cluster ages, its gas fraction changes with time due to the effects of thermal conduction. We have shown that this scatter depends on the amount of conduction. In each of the five initial cluster profiles studied, conduction levels greater than 10% of Spitzer conduction result in a scatter greater than that observed by [Mantz et al.(2014)]. It is therefore our conclusion that conduction values greater than 10% of Spitzer are unlikely, based on these results.

This is an initial pilot study. These results are only qualitative, but are also conservative. Our results apply to large-scale isotropic conduction along the radial direction, outside of the cluster core and away from special conduction regions (such as cold fronts). Our results suggest that thermal conduction is strongly suppressed, to a level below the 30 % expected in the simple case of randomly tangled magnetic fields. This suggests that either the field orientation is preferentially tangled, or there is suppression of thermal conduction along the field lines by small-scale plasma instabilities [Schekochikhin, et al.(2008)], [Kunz(2010)]. More stringent constraints may be obtained by using cosmological simulations including thermal conduction and the selection of relaxed clusters (similar to [Mantz et al.(2014)]).

Bibliography

[Arnaud, et al.(2011)] Arnaud, K., et al., Introduction in *Handbook of X-ray Astronomy*, Arnaud, K., Smith, R., and Siemiginowska, A., eds, 2011, Cambridge University Press

[Blackburn(1995)] Blackburn, J. K., 1995, in ASP Conf. Ser., Vol. 77, Astronomical Data Analysis Software and Systems IV, ed. R. A. Shaw, H. E. Payne, and J. J. E. Hayes (San Francisco: ASP), 367

[Branch(1998)] Branch, D. 1998, *ARA&A*, 36, 17

[Brown(2011)] Brown, P. J., et al. 2011, arXiv:1110.2538

[Burrows(2005)] Burrows, D. N., et al. 2005, Space Sci. Rev., 12, 165

[Carilli & Taylor(2002)] Carilli, C. L., & Taylor, G. B., 2002, *ARA&A* 40, 319

[Chevalier(1990)] Chevalier, R. A. 1990, in Supernovae, ed. A. G. Petschek (New York, NY: Springer-Verlag), 91

[Chevalier & Fransson(2003)] Chevalier, R. A., & Fransson, C. 2003, in Supernovae and Gamma-Ray Bursters, ed. K. Weiler (New York, NY: Springer-Verlag), 171

[Dickey & Lockman(1990)] Dickey & Lockman, 1990, *ARA&A*, 28, 215

[DiStefano(2010a)] DiStefano, R. 2010, *ApJ*, 712, 728

[DiStefano(2010b)] DiStefano, R. 2010, *ApJ*, 719, 474

[Eck et al.(1995)] Eck, C. R., Cowen, J. J., Roberts, D. A., Boffi, F. R., & Branch, D. 1995, *ApJL*, 451, L53

[Ettori & Fabian(2000)] Ettori, S., & Fabian, A., 2000, *MNRAS*, 317, L57

[Feretti & Giovannini(2008)] Feretti, L., & Giovannini, G., in Lect. Notes Phys. **740**, 143-176 (2008)

[Fransson et al.(1996)] Fransson, C., Lundqvist, P., and Chevalier, R. 1996, *ApJ*, 461, 993

[Gehrels et al.(2004)] Gehrels, N. et al. 2004, *ApJ*, 611, 1005.

[Gilfanov & Bogdán(2010)] Gilfanov, M., & Bogdán, Á. 2010, *Nature*, 463, 924

[Gruzinov(2002)] Gruzinov, A., 2002, arXiv:astro-ph/0203031

[Hamuy et al.(2003)] Hamuy, M., et al., 2003, *Nature*, 424, 651

[Hancock et al.(2011)] Hancock, P., Gaensler, B. M., & Murphy, T. 2011, *ApJ*, 735, L35

[Hayden et al.(2010)] Hayden, B. T., et al. 2010, *ApJ*, 722, 1691

[Hillebrandt & Niemeyer(2000)] Hillebrandt, W., & Niemeyer, J. 2000, *ARA&A*, 38, 191

[Hughes et al.(2007)] Hughes, J. P., et al. 2007, *ApJ*, 670, 1260

[Iben & Tutukov(1984)] Iben, I., & Tutukov, A. V. 1984, *ApJS*, 54, 335

[Immler et al.(2001)] Immler, S., Aschenbach, B., & Daniel Wang, Q. 2001, *ApJ*, 561, L107

[Immler et al.(2006)] Immler, S., et al. 2006, *ApJ*, 648, L119

[Jones et al.(2008)] C. Jones et al *Dynamics of the Hot Intracluster Medium*, Lect. Notes Phys. **740**, 31-69 (2008)

[Kasen(2010)] Kasen, D., 2010, *ApJ*, 708, 1025

[Kunz(2010)] Kunz, M. W., et al., 2011, *MNRAS*, 410, 2446

[Livio & Riess(2003)] Livio, M., & Riess, A. G. 2003, *ApJL*, 594, L93

[Mantz et al.(2014)] Mantz, A. B., et al. 2014, *MNRAS* 440, 2077

[Maoz et al.(2010)] Maoz, D., Sheren, K., & Gal-Yam, A. 2010, *ApJ*, 722, 1879

[Markevitch(1998)] Markevitch, M., et al., 1998 *ApJ* 503, 77

[Markevitch, et al.(2000)] Markevitch, M., et al., 2000 *ApJ* 541, 542

[Markevitch & Vikhlinin(2007)] Markevitch, M., & Vikhlinin, A., 2007 *Ph Rep* 443, 1

[Navarro et al.(1996)] Navarro, J. F., Frenk, C. S., & White, S. D., 1996, *ApJ* 462, 563

[Nomoto(1982)] Nomoto, K. 1982, *ApJ*, 253, 798

[Nomoto(1984)] Nomoto, K. 1984, *ApJ*, 286, 644

[Nomoto et al.(1997)] Nomoto, K., Iwamoto, K., & Kishimoto, N. 1997, Science, 276, 1378

[Panagia et al.(2006)] Panagia, N., Van Dyk, S. D., Weiler, K. W., Sramek, R. A., Stockdale, C. J., & Murata, K. P. 2006, *ApJ*, 646, 369

[Perlmutter et al.(1999)] Perlmutter, S., et al. 1999, *ApJ*, 517, 565

[Press & Schechter(1974)] Press, W. H., & Schechter, P., 1974, *ApJ* 187, 425

[Riess et al.(1998)] Riess, A. G., et al. 1998, AJ, 116, 1009

[Sarazin(1988)] Sarazin, C., 1988, *X-ray Emission from Clusters of Galaxies*

[Sarazin(2008)] Sarazin, c., 2008, in *A Pan-Chromatic View of Clusters of Galaxies and their Large Scale Structures*, Plionis, M., Lopez-Cruz, O., and Hughes, D., eds.

[Schekochikhin, et al.(2008)] Schekochikhin, et al. 2008, *PRL*, 100, 081301

[Schlegel & Petre(1993)] Schlegel, E. M., & Petre, R. 1993, *ApJL*, 412, L29

[Schwartz(2011)] Schwartz, D. A., 2011, in *Handbook of X-ray Astronomy*, Arnaud, K., et al., eds. Cambridge University Press

[SC(2008)] Seward, F. D., and Charles, P. A., 2010, *Exploring the X-ray Universe*, Cambridge University Press

[Spitzer(1958)] Spitzer, L., & Harm, R., 1958 *ApJ* 127, 544

[Sternberg et al.(2011)] Sternberg, A., et al. 2011, arXiv:1108.3664

[Sunyaev(1971)] Sunyaev, R. A., 1971, *A&A* 12, 190

[van Kerkwijk et al.(2010)] van Kerkwijk, M. H., Chang, P., & Justham, S. 2010, *ApJL*, 722, L157

[Vikhlinin et al.(2001)] Vikhlinin, A., et al. 2001, *ApJ*, 551, 160

[Vikhlinin et al.(2005)] Vikhlinin, A., et al. 2005, *ApJ*, 628, 655

[Vikhlinin et al.(2006)] Vikhlinin, A., et al. 2006, *ApJ*, 640, 691

[Webbink(1984)] Webbink, R. F. 1984, *ApJ*, 277, 355

[Whelen & Iben(1973)] Whelen, J., & Iben, I. 1973, *ApJ*, 186, 1007

[White et al.(1993)] White, S. D. M., 1993, *Nature* 366, 429

[Woosley & Weaver(1986)] Woosley, S. E., & Weaver, T. A. 1986, *ARA&A*, 24, 205

[Yungelson et al.(1995)] Yungelson, L., et al. 1995, *ApJ*, 447, 656